Article

ADAR1 prevents autoinflammation by suppressing spontaneous ZBP1 activation

https://doi.org/10.1038/s41586-022-04974-w

Received: 2 October 2021

Accepted: 13 June 2022

Published online: 20 July 2022

Check for updates

Richard de Reuver[1,2,9], Simon Verdonck[1,2,9], Evelien Dierick[1,2], Josephine Nemegeer[1,2], Eline Hessmann[1,2], Sadeem Ahmad[3,4], Maude Jans[1,2], Gillian Blancke[1,5], Filip Van Nieuwerburgh[6,7], Alexander Botzki[8], Lars Vereecke[1,5], Geert van Loo[1,2], Wim Declercq[1,2], Sun Hur[3,4], Peter Vandenabeele[1,2] & Jonathan Maelfait[1,2]✉

The RNA-editing enzyme adenosine deaminase acting on RNA 1 (ADAR1) limits the accumulation of endogenous immunostimulatory double-stranded RNA (dsRNA)[1]. In humans, reduced ADAR1 activity causes the severe inflammatory disease Aicardi–Goutières syndrome (AGS)[2]. In mice, complete loss of ADAR1 activity is embryonically lethal[3–6], and mutations similar to those found in patients with AGS cause autoinflammation[7–12]. Mechanistically, adenosine-to-inosine (A-to-I) base modification of endogenous dsRNA by ADAR1 prevents chronic overactivation of the dsRNA sensors MDA5 and PKR[3,7–10,13,14]. Here we show that ADAR1 also inhibits the spontaneous activation of the left-handed Z-nucleic acid sensor ZBP1. Activation of ZBP1 elicits caspase-8-dependent apoptosis and MLKL-mediated necroptosis of ADAR1-deficient cells. ZBP1 contributes to the embryonic lethality of *Adar*-knockout mice, and it drives early mortality and intestinal cell death in mice deficient in the expression of both ADAR and MAVS. The Z-nucleic-acid-binding Zα domain of ADAR1 is necessary to prevent ZBP1-mediated intestinal cell death and skin inflammation. The Zα domain of ADAR1 promotes A-to-I editing of endogenous Alu elements to prevent dsRNA formation through the pairing of inverted Alu repeats, which can otherwise induce ZBP1 activation. This shows that recognition of Alu duplex RNA by ZBP1 may contribute to the pathological features of AGS that result from the loss of ADAR1 function.

ADAR1-deficient ($Adar^{-/-}$) mice develop an MDA5-mediated type I interferon (IFN-I) response, which causes death between embryonic day (E) 11.5 and E12.5 (refs. [3,5,6,13–15]). Genetic-mediated removal of MDA5 or the downstream signalling protein MAVS rescues the embryonic lethality of $Adar^{-/-}$ mice. However, mice deficient in both ADAR1 and MDA5 or in ADAR1 and MAVS still die during the first weeks after birth[13,14,16] (Fig. 1a). This suggests that ADAR1 limits the spontaneous activation of other immune sensors. In addition to binding dsRNA through three consecutive dsRNA-binding motifs, ADAR1 can interact with left-handed dsRNA or dsDNA in the Z conformation through its amino-terminal Zα domain[17,18]. We therefore hypothesized that ADAR1 may also suppress activation of the Z-nucleic-acid sensor ZBP1. To test this hypothesis, we generated $Adar^{-/-}Mavs^{-/-}$ mice that express ZBP1 containing two amino acid substitutions in the two N-terminal Zα domains (N46A and Y50A in the first Zα1 domain and N122A and Y126A in the second Zα2 domain)[19], which impair ZBP1 binding to Z-nucleic acids[20,21] (Extended Data Fig. 1a). Sanger sequencing of *Htr2c*, *Mad2l1* and *Rpa1* mRNA, known substrates of ADAR1 (refs. [3,6]), confirmed the complete lack of ADAR1 activity in these mice (Extended Data Fig. 1b). Despite lower birth weights than their ADAR1-proficient littermates, $Adar^{-/-}Mavs^{-/-}Zbp1^{Zα1α2/Zα1α2}$ pups gained weight more rapidly than $Adar^{-/-}Mavs^{-/-}Zbp1^{+/+}$ or $Adar^{-/-}Mavs^{-/-}Zbp1^{+/Zα1α2}$ mice (Extended Data Fig. 1c). Around half of the $Adar^{-/-}Mavs^{-/-}Zbp1^{Zα1α2/Zα1α2}$ mice survived until about 20 weeks of life; however, they remained smaller than their control littermates (Fig. 1a and Extended Data Fig. 1d). Spontaneous ZBP1 activation causes necroptotic cell death of keratinocytes or intestinal epithelium, which results in sterile autoinflammation[22–26]. Moreover, intestinal homeostasis is disrupted in $Adar^{-/-}Mavs^{-/-}$ mice[13,16]. As $Adar^{-/-}Mavs^{-/-}$ mice did not develop skin lesions, we investigated whether ZBP1-mediated cell death causes intestinal dysfunction in *Adar* and *Mavs* double-knockout mice. TdT-mediated dUTP nick end-labelling (TUNEL) revealed mild cell death in the ilea of 1-week-old *Adar* and *Mavs* double-knockout mice that express wild-type ZBP1, which was absent in ilea from $Adar^{-/-}Mavs^{-/-}Zbp1^{Zα1α2/Zα1α2}$ mice (Extended Data Fig. 1e,f). At 5 weeks of age, however, the ilea of $Adar^{-/-}Mavs^{-/-}Zbp1^{Zα1α2/Zα1α2}$ mice accumulated a substantial number of dead cells. By contrast, colon tissues from 5-week-old $Adar^{-/-}Mavs^{-/-}Zbp1^{Zα1α2/Zα1α2}$ mice were devoid of TUNEL-positive cells, whereas colons of 1-week-old $Adar^{-/-}Mavs^{-/-}Zbp1^{+/Zα1α2}$ mice displayed extensive cell death (Fig. 1b,c). The differential phenotypic rescue across the intestine is consistent with

[1]VIB-UGent Center for Inflammation Research, Ghent, Belgium. [2]Department of Biomedical Molecular Biology, Ghent University, Ghent, Belgium. [3]Department of Biological Chemistry and Molecular Pharmacology, Harvard Medical School, Howard Hughes Medical Institute, Boston, MA, USA. [4]Program in Cellular and Molecular Medicine, Boston Children's Hospital, Howard Hughes Medical Institute, Boston, MA, USA. [5]Department of Internal Medicine and Pediatrics, Ghent University, Ghent, Belgium. [6]NXTGNT, Faculty of Pharmaceutical Sciences, Ghent University, Ghent, Belgium. [7]Laboratory of Pharmaceutical Biotechnology, Faculty of Pharmaceutical Sciences, Ghent University, Ghent, Belgium. [8]VIB Bioinformatics Core, VIB, Ghent, Belgium. [9]These authors contributed equally: Richard de Reuver, Simon Verdonck. ✉e-mail: jonathan.maelfait@irc.vib-ugent.be

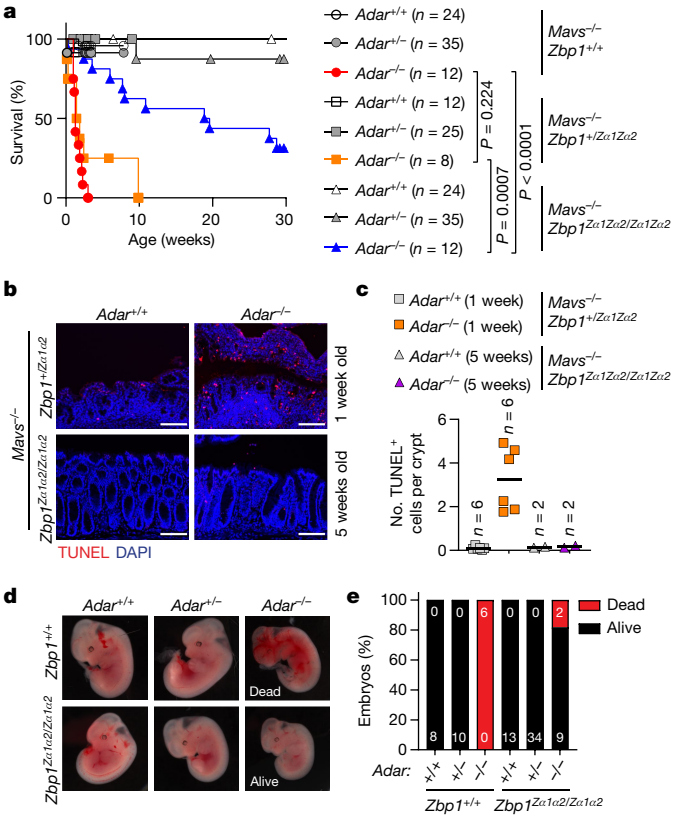

Fig. 1 | ZBP1 causes early postnatal lethality of *Adar* and *Mavs* double-knockout mice and accelerates the death of *Adar*$^{-/-}$ embryos. **a**, Kaplan–Meier survival curves of mice with the indicated genotypes. *P* values were calculated using log-rank test. The numbers of mice (*n*) that were analysed per genotype are indicated. **b**,**c**, TUNEL assay of colon sections from 1- or 5-week-old *Adar*$^{-/-}$*Mavs*$^{-/-}$ mice expressing a Zα domain mutant ZBP1 from one (*Zbp1*$^{+/Zα1α2}$) or two (*Zbp1*$^{Zα1α2/Zα1α2}$) alleles. **b**, Representative images of colon sections. Scale bars, 100 µm. **c**, Quantification of TUNEL^{+} cells per crypt. Lines represent the mean, and each data point represents an individual mouse. The numbers of mice (*n*) that were analysed per genotype are indicated. **d**, Macroscopic pictures of E12.5 embryos of the indicated genotypes. **e**, Viability of E12.5 embryos based on the presence or absence of a heartbeat. Numbers in the bar chart represent the number of embryos that were analysed per genotype.

the redundant role of ZBP1 in the ileum and its non-redundant role in the colon[27]. ADAR1 deficiency results in impaired development of neutrophils, T cells and B cells, which occur independently of MDA5 and MAVS[13,16,28]. We confirmed that spleens of newborn *Adar*$^{-/-}$*Mavs*$^{-/-}$ pups had reduced overall cellularity and contained fewer T and B cells, albeit independently of the *Zbp1* genotype (Extended Data Fig. 2a,d). However, *Adar*$^{-/-}$*Mavs*$^{-/-}$*Zbp1*$^{+/+}$ and *Adar*$^{-/-}$*Mavs*$^{-/-}$*Zbp1*$^{+/Zα1α2}$ mice had almost no neutrophils, and this phenotype was restored in mice expressing Zα domain mutant ZBP1, even in mice that reached 20 weeks of age (Extended Data Figs. 2a–c and 3b,c). In agreement with previous results showing that disrupted erythroid development due to loss of ADAR1 function is driven by MDA5 and MAVS signalling[3,15,29], we observed normal red blood cell development in *Adar*$^{-/-}$*Mavs*$^{-/-}$*Zbp1*$^{Zα1α2/Zα1α2}$ mice, although white blood cell counts were severely reduced (Extended Data Fig. 3a–c). This decrease was caused by a specific loss of lymphoid cells, including B cells, T cells and natural killer T cells, whereas absolute numbers of myeloid cells remained unaffected (Extended Data Fig. 3b,c). These findings show that spontaneous ZBP1 activation in *Adar* and *Mavs* double-knockout mice results in intestinal cell death and impaired neutrophil development. Moreover, progressive loss of lymphoid cells occurs independently of MDA5, MAVS and ZBP1 and is possibly driven by other dsRNA sensors such as PKR and/or OAS proteins[30].

To test whether ZBP1 contributes to the death of ADAR1-deficient embryos, we monitored the viability of *Adar*$^{-/-}$*Zbp1*$^{Zα1α2/Zα1α2}$ embryos at different stages during development (Extended Data Fig. 3e). In contrast to *Adar*$^{-/-}$*Zbp1*$^{+/+}$ embryos, which all died at E12.5, most *Adar*$^{-/-}$*Zbp1*$^{Zα1α2/Zα1α2}$ embryos appeared normal and approximately 80% were still alive (Fig. 1d,e). *Adar*$^{-/-}$ embryos displayed a ZBP1-independent IFN-I response and increased expression of inflammatory genes (Extended Data Fig. 3d,f,g). We recovered only one *Adar*$^{-/-}$*Zbp1*$^{Zα1α2/Zα1α2}$ embryo at E13.5, which was not viable (Extended Data Fig. 3e). This result shows that loss of ZBP1 function extended the lifespan of these embryos by a maximum of one gestational day.

The Zα domain of ADAR1 limits ZBP1 activation

The Zα domain-containing p150 isoform of ADAR1, but not the p110 isoform, inhibits MDA5–MAVS-mediated immune activation and lethality in mice[13,31]. To determine whether the Zα domain of ADAR1-p150 is physiologically important in the control of spontaneous ZBP1 activation, we tested whether ZBP1 contributed to the pathogenesis of *Adar* knock-in mice that carry an *Adar* allele encoding an ADAR1 protein in which the Zα domain is mutated (N175A and Y179A, *Adar*^{Zα}) paired with a second *Adar* null allele. As previously shown[10], all *Adar*$^{Zα/–}$*Zbp1*$^{+/+}$ mice died within 2 days, whereas more than half of the *Adar*$^{Zα/–}$*Zbp1*$^{Zα1α2/Zα1α2}$ mice reached at least 18 weeks of age (Fig. 2a and Extended Data Fig. 4a). The surviving mice remained smaller compared with their *Adar* wild-type littermates (Extended Data Fig. 4b,c). Caeca and colons of newborn *Adar*$^{Zα/–}$ mice contained aggregates of necrotic tissue, which was absent in *Adar*$^{Zα/–}$*Zbp1*$^{Zα1α2/Zα1α2}$ pups (Extended Data Fig. 4d). In accordance, we detected TUNEL-positive cells in the intestines of *Adar*$^{Zα/–}$ mice, which was reduced in mice with a ZBP1 Zα domain mutant background (Fig. 2b,c). Quantitative reverse transcription PCR (RT–qPCR) analysis of IFN-stimulated genes (ISGs) and inflammatory genes in intestinal, brain and lung tissues showed that ZBP1 partially contributed to the increased expression of a subset of these genes (Fig. 2d and Extended Data Fig. 4e,f). As such, ZBP1 may directly regulate the expression of specific ISGs and inflammatory genes. Alternatively, ZBP1-mediated cell death may indirectly contribute to the increased expression of these genes through the release of damage-associated molecular pattens from dying cells and subsequent activation of other immune sensors. In contrast to the partial rescue of *Adar*$^{Zα/–}$*Zbp1*$^{Zα1α2/Zα1α2}$ mice, crossing *Adar*$^{Zα/–}$ mice into a MAVS-deficient background completely prevented intestinal cell death and the induction of ISG expression, including ZBP1 (Fig. 2b–d and Extended Data Fig. 4e), which is in line with the complete rescue of *Adar*$^{Zα/–}$*Mavs*$^{–/–}$ mice from lethality[10]. Moreover, the survival of *Adar*$^{Zα/–}$*Zbp1*$^{Zα1α2/Zα1α2}$ mice was more pronounced in a *Mavs* heterozygous state (Extended Data Fig. 4g). This result indicates that MAVS signalling potentiates ZBP1-induced pathology in *Adar*$^{Zα/–}$ mice, probably by inducing the expression of *Zbp1* itself.

To further validate whether Z-nucleic-acid binding to ADAR1 is pivotal in restricting ZBP1 activation, we crossed mice that express a mutant ADAR1 Zα domain to keratinocyte-specific *Ripk1*-knockout mice (*Ripk1*^{EKO}). The recognition of endogenous Z-nucleic acids by ZBP1 causes RIPK3–MLKL-mediated necroptosis of RIPK1-deficient keratinocytes, which results in skin inflammation[22,23]. Here, we did not retrieve any homozygous *Adar*$^{Zα/Zα}$*Ripk1*^{EKO} mice, which suggests that this gene combination is lethal in utero. The introduction of only one Zα domain mutant *Adar* allele in the *Ripk1*^{EKO} background, however, accelerated the development of macroscopically visible skin lesions, enhanced thickening of the epidermis and increased influx of inflammatory cells (Fig. 2e–g and Extended Data Figs. 5a,b and 6). Together, these data demonstrate that an intact Zα domain of ADAR1 is crucial for inhibiting spontaneous ZBP1 activation.

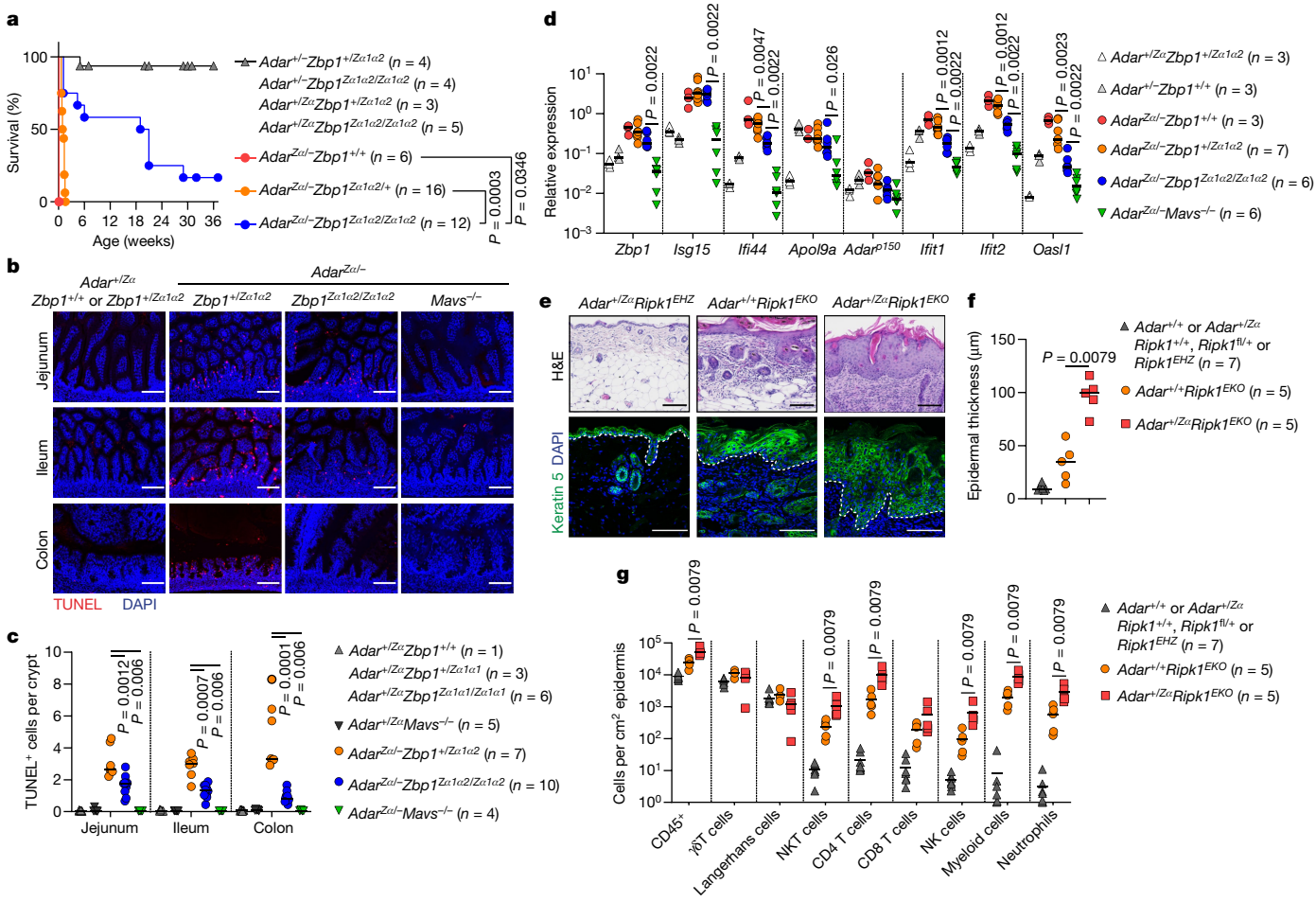

Fig. 2 | The Zα domain of ADAR1-p150 is crucial for the prevention of spontaneous ZBP1 activation. a, Kaplan–Meier survival curves of mice with the indicated genotypes. *P* values were calculated using log-rank test. The numbers of mice (*n*) that were analysed per genotype are indicated. **b**,**c**, TUNEL assay of intestinal tissue sections from the jejunum, ileum and colon of 1-day-old pups with the indicated genotypes. **b**, Representative images of jejunum, ileum and colon sections. Scale bars, 100 μm. **c**, Quantification of TUNEL$^+$ cells per crypt. **d**, RT–qPCR analysis of the indicated ISGs analysed in whole intestine samples of 1-day-old pups with the indicated genotypes. **e**–**g**, Skin analysis of epidermis-specific *Ripk1*-knockout mice (*Ripk1*^{EKO}) carrying heterozygous ADAR1 Zα domain mutant alleles (*Adar*$^{+/Zα}$) or expressing wild-type ADAR1. Littermate offspring containing one or two functional *Ripk1* alleles (*Ripk1*$^{+/+}$, *Ripk1*$^{fl/+}$) or heterozygously expressing a functional *Ripk1* allele in the epidermis (*Ripk1*^{EHZ}) did not develop lesions and are shown as controls. **e**, Skin sections of 21-day-old mice were stained with H&E or keratin 5 and DAPI. Dashed line depicts the border between the epidermis and dermis. Scale bars, 100 μm. **f**, Quantification of epidermal thickness on H&E-stained sections shown in **e**. **g**, Flow cytometry analysis of leukocyte (CD45$^+$) composition of the epidermis of 21-day-old mice with the indicated genotypes. The gating strategy is outlined in Extended Data Fig. 6. NK cells, natural killer cells; NKT cells, natural killer T cells. Lines in **c**, **d**, **f** and **g** represent the mean, and each data point in **c**, **d**, **f** and **g** represents an individual mouse. The numbers of mice (*n*) that were analysed per genotype are indicated. *P* values were calculated using Mann–Whitney test.

ADAR1 inhibits ZBP1-induced cell death

Virus-induced ZBP1 activation leads to the recruitment of RIPK3, which induces parallel pathways of RIPK1–FADD–caspase-8-mediated apoptosis and MLKL-mediated necroptosis[32,33]. To determine which signalling pathways cause death of ADAR1-deficient cells, we treated primary mouse lung fibroblasts with IFNα to induce ZBP1 expression. To exclude confounding effects of spontaneous MDA5 and MAVS and/or TNF signalling on cell survival, we cultured *Adar* and *Mavs* double-knockout cells with TNF-neutralizing antibodies. Stimulation of ADAR1-deficient fibroblasts with IFNα and the protein synthesis inhibitor cycloheximide (CHX), which enhances TNF-induced cell death by preventing the translation of cFLIP$_L$ (refs. [34,35]), induced ZBP1-mediated cell death (Fig. 3a and Extended Data Fig. 7a). Western blotting revealed that ZBP1 induced both proteolytic activation of caspase-8 and phosphorylation of MLKL (Fig. 3b). This result shows that CHX treatment sensitizes ADAR1-deficient fibroblasts to ZBP1-mediated apoptosis and necroptosis, which may be held in check by the anti-apoptotic and anti-necroptotic functions of cFLIP$_L$ (refs. [36,37]). Caspase-8 inhibition sensitizes cells to ZBP1-mediated necroptosis[19,23]. Accordingly, treatment of fibroblasts pre-stimulated with IFNα with the pan-caspase inhibitor zVAD-FMK greatly accelerated ZBP1-dependent necroptosis of *Adar*-knockout cells (Extended Data Fig. 7b,c) and of lung fibroblasts isolated from *Adar*$^{Zα/−}$*Mavs*$^{−/−}$ mice, which hemizygously express Zα domain mutant ADAR1 (Extended Data Fig. 7g,h). By contrast, ZBP1 activation after infection with herpes simplex virus 1 (HSV1) expressing a RIP homotypic interaction motif (RHIM) mutant ICP6 protein, which is unable to block ZBP1-driven necroptosis[38], induced ZBP1-mediated necroptosis independently of ADAR1 (Extended Data Fig. 7d). As controls, apoptosis and necroptosis induced by TNF and CHX or by TNF and zVAD-FMK proceeded independently of the *Adar* and/or *Zbp1* genotypes (Extended Data Fig. 7e,f,i,j). Intestinal crypts of *Adar*$^{Zα/−}$ mice, but not of those expressing Zα domain mutant ZBP1, stained positive for cleaved caspase-8, which provides confirmation that reduced ADAR1 activity causes ZBP1-induced caspase-8 activation in vivo (Fig. 3c and Extended Data Fig. 9a).

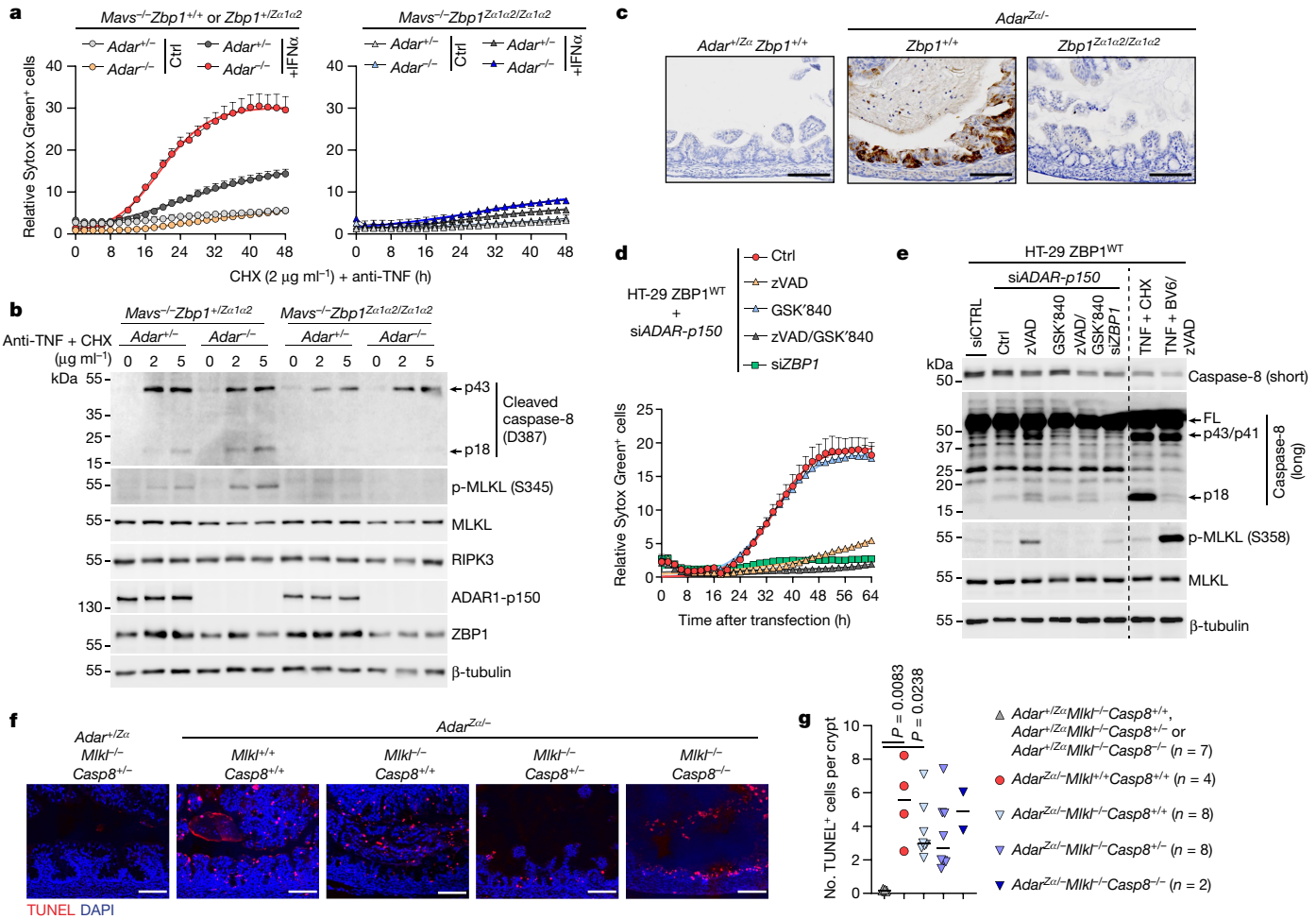

Fig. 3 | Loss of ADAR1 function induces ZBP1-mediated caspase-8-dependent apoptosis and MLKL-dependent necroptosis. a,**b**, Primary mouse lung fibroblasts of the indicated genotypes were stimulated with 200 U ml^{-1} IFNα for 16 h or left untreated (Ctrl). Next, cells were treated with 2 μg ml^{-1} or 5 μg ml^{-1} CHX and 1 μg ml^{-1} anti-mouse TNF antibody. **a**, Cell death was quantified by measuring relative Sytox Green uptake every 2 h. **b**, Immunoblot related to **a** and Extended Data Fig. 7a. Samples were collected 16 h after treatment. **c**, Representative images of cleaved caspase-8 (D387) staining of colon sections of mice with the indicated genotypes. Scale bars, 100 μm. $n = 3$ mice per genotype were analysed. **d**,**e**, Human HT-29 cells stably expressing wild-type human ZBP1 (ZBP1^{WT}) were transfected with control siRNAs (siCTRL) or siRNAs targeting the p150 isoform of *ADAR* (si*ADAR-p150*) and *ZBP1* (si*ZBP1*). After 5 h, cells were treated with 20 μM zVAD-FMK (zVAD) and/or 3 μM GSK'840. **d**, Cell death was analysed as in **a**. **e**, Protein expression was analysed 30 h after transfection. Controls samples were treated with 30 ng ml^{-1} human TNF, 5 μM BV6 and 20 μM zVAD-FMK for 3 h or with 30 ng ml^{-1} TNF and 20 μg ml^{-1} CHX for 6 h. FL, full length. **f**,**g**, TUNEL assay of colon sections from 1-day-old mice with the indicated genotypes. **f**, Representative images of colon sections. Scale bars, 100 μm. **g**, Quantification of TUNEL^{+} cells per crypt. Lines represent the mean, and each data point represents an individual mouse. *P* values were calculated using Mann–Whitney test. Data in **a** and **d** are representative of three independent experiments. Fitted lines represent a logistic growth fit, and data points show the mean and s.e.m. For gel source data, see Supplementary Fig. 1.

To explore these findings in human cells, we used siRNAs to deplete the expression of ADAR1 or only the Zα-domain-containing ADAR1-p150 isoform (Extended Data Fig. 8a) in HT-29 colorectal adenocarcinoma cell lines transduced with either wild-type human ZBP1 or Zα domain mutant ZBP1 (N46A and Y50A in the first Zα1 domain and N141A and Y145A in the second Zα2 domain). Consistent with the mouse data, depletion of ADAR1 expression triggered death in cells expressing wild-type ZBP1 but not those expressing Zα-domain mutant ZBP1 (Extended Data Fig. 8b). As controls, caspase-8-mediated apoptosis induced by TNF and CHX, and necroptosis induced by combined treatment with TNF, the SMAC mimetic BV6 and zVAD-FMK, proceeded with similar kinetics in both cell lines (Extended Data Fig. 8c,d). Specific depletion of ADAR1-p150 expression caused ZBP1-mediated cell death with similar kinetics to that of combined ADAR1-p110 and ADAR1-p150 depletion, which indicates that the p150 isoform is the main inhibitor of ZBP1 activation (Fig. 3d and Extended Data Fig. 8b,e). Treatment with zVAD-FMK inhibited cell death, which demonstrates that ADAR1 and ADAR1-p150 depletion in human cells induces ZBP1-dependent apoptosis. This was further supported by the presence of cleaved caspase-8 (Fig. 3d,e and Extended Data Fig. 8e,f). Prolonged zVAD-FMK treatment caused a switch from apoptosis to necroptosis after transfection with *ADAR*-specific or *ADAR1-p150*-specific siRNA. This was confirmed by the presence of MLKL phosphorylation and by inhibition of this effect when cells were treated with the RIPK3 kinase inhibitor GSK'840 (Fig 3d,e and Extended Data Fig. 8e,f). Sole inhibition of RIPK3 by GSK'840 treatment without zVAD-FMK had no effect on cell death following ADAR1 or ADAR-p150 depletion, which demonstrates that the primary mode of cell death downstream of human ZBP1 is apoptosis. The RHIM-containing proteins RIPK1 and RIPK3, but not TRIF (also known as TICAM1), contributed to caspase-8-mediated apoptosis caused by ADAR1-p150 depletion in human cells expressing ZBP1 (Extended Data Fig. 8g,h). In summary, these data demonstrate that the Z-nucleic-acid-binding p150 isoform of ADAR1 limits ZBP1-mediated cell death in mouse and human cells.

Given the central role of RIPK3 in the induction of ZBP1-mediated caspase-8-dependent apoptosis and MLKL-dependent necroptosis during virus infection[32,33], we generated *Adar*$^{Zα/-}$ mice in a RIPK3-deficient background. In contrast to the prolonged survival of *Adar*$^{Zα/-}$*Zbp1*$^{Zα1α2/Zα1α2}$ mice (Fig. 2a), we observed only a minor survival advantage in mice in which one or two *Ripk3* alleles were deleted (Extended Data Fig. 9b,c). In the absence of RIPK3, ZBP1 may directly recruit RIPK1 to induce caspase-8-mediated apoptosis[32,33]. We therefore generated *Adar*$^{Zα/-}$ mice in which both *Mlkl* and *Casp8* were knocked out to abrogate both the necroptotic and the extrinsic apoptotic pathways. Notably, none of the resulting *Adar*$^{Zα/-}$*Mlkl*$^{-/-}$*Casp8*$^{-/-}$ mice survived beyond 2 days of birth (Extended Data Fig. 8d–h). Although intestinal cell death was reduced in *Adar*$^{Zα/-}$*Zbp1*$^{Zα1α2/Zα1α2}$ mice (Fig. 2b), we still detected substantial numbers of TUNEL-positive cells in the colons of *Adar*$^{Zα/-}$*Mlkl*$^{-/-}$*Casp8*$^{-/-}$ pups (Fig. 3f,g). Future studies will address how these mice are not rescued from lethality. It is possible that ZBP1 directly activates other cell death pathways or that caspase-8 and/or MLKL dampen cell death signals that originate from other immune sensors in *Adar*$^{Zα/-}$ mice.

Alu duplex RNA activates ZBP1

We next sought to understand how loss of Zα-domain-dependent ADAR1 functions cause spontaneous activation of ZBP1. To this end, we performed high-coverage mRNA sequencing to analyse the A-to-I editing profile of repeat elements within mRNA transcripts in ADAR1 Zα domain mutant mouse fibroblasts and in human HEK293 cells[10]. We used primary lung fibroblasts from *Adar*$^{Zα/-}$*Mavs*$^{-/-}$ mice to minimize the effects of differential expression due to spontaneous MDA5 and MAVS activation. Cells were stimulated with IFNα to induce ADAR1-p150 expression and editing by this isoform. As expected, IFNα stimulation increased overall editing of repeats in mouse fibroblasts (Extended Data Fig. 10a). Mouse SINE Alu, B2 and B4 elements and human Alu repeats constituted the majority of edited repeat elements (Fig. 4b Extended and Data. 10b). In contrast to previous studies reporting that a subset of editing sites may be specifically regulated by the Zα domain of ADAR1 (refs. [8–10]), our high coverage approach, which enabled us to detect sparsely edited adenosine residues across whole repeat sequences, did not reveal a substantial ADAR1 genotype-dependent bias in A-to-I editing (Fig. 4b and Extended Data Fig. 10c). Instead, loss of Zα-domain-mediated interactions of ADAR1 with Z-nucleic acids led to an overall reduction in the quality of repeat editing (Fig. 4a,c). Complete editing of an AluSp element that was most significantly affected by a mutation in the ADAR1 Zα domain and its nearest inverted AluSx1 repeat created 11 additional bulges within the predicted AluSp–AluSx1 RNA duplex and substantially lowered its stability (Fig. 4c and Extended Data Fig. 10d–f). Alu–Alu hybrids are potent agonists of MDA5 when ADAR1 activity is lost[39,40]. To test whether these dsRNA structures could also stimulate ZBP1, we transfected in vitro transcribed Alu–Alu hybrids from the 3′ untranslated regions (UTRs) of the *NICN1* and *BPNT1* mRNAs into HT-29 cells expressing human ZBP1. Both Alu–Alu hybrids strongly induced ZBP1-dependent cell death, which depended on intact ZBP1 Zα domains and could be inhibited by zVAD-FMK (Fig. 4d,e and Extended Data Fig. 10g). Similar to the siRNA-mediated ADAR1 depletion experiments (Fig. 3d and Extended Data Fig. 8e), prolonged ZBP1 stimulation and caspase blockade triggered cell death that was blocked by the RIPK3 kinase inhibitor GSK′840 (Fig. 4e and Extended Data Fig. 10g).

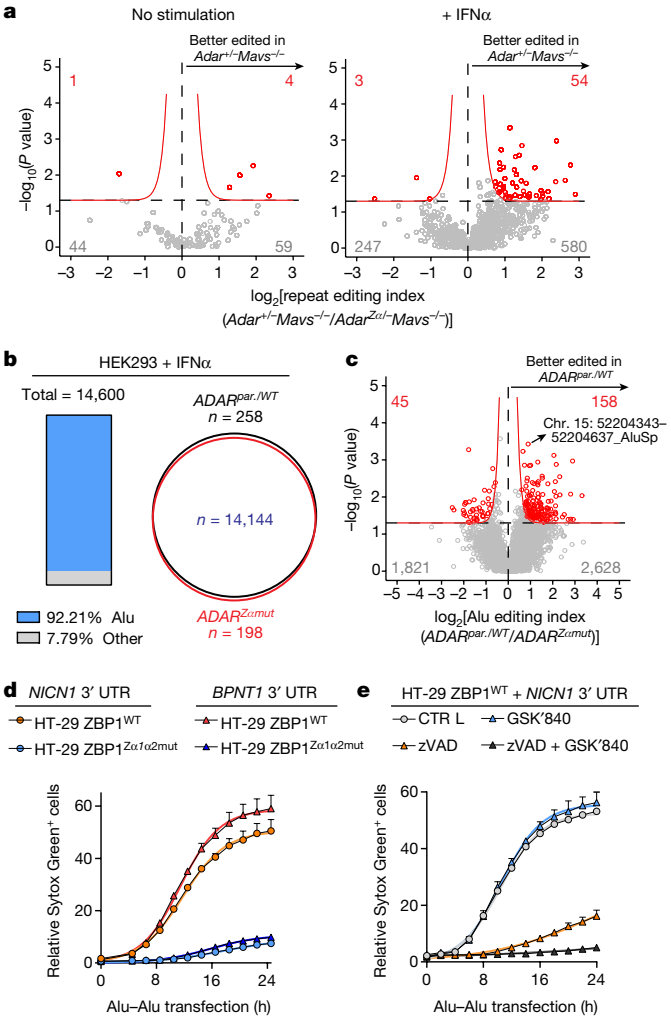

Fig. 4 | Alu duplex RNA stimulates ZBP1-dependent cell death. a, Primary lung fibroblasts from *Adar*$^{+/-}$*Mavs*$^{-/-}$ and *Adar*$^{Zα/-}$*Mavs*$^{-/-}$ mice were stimulated for 16 h with 200 U ml^{-1} IFNα or left untreated. The repeat editing index was calculated using all identified A-to-I editing sites within a single repeat element. **b**, Wild-type (HEK293 parental cells and two wild-type clones; *ADAR*$^{par./WT}$) and *ADAR*^{Zαmut} HEK293 clones were stimulated for 16 h with 1,000 U ml^{-1} IFNα. Repeat families that underwent A-to-I editing in three independent HEK293 clones are visualized in the boxplot. The Venn diagram illustrates the number of repeat elements that displayed genotype-specific A-to-I editing or those that were detected in both groups. **c**, Volcano plot demonstrating the differential A-to-I editing activity on Alu elements comparing wild-type and *ADAR*^{Zαmut} HEK293 cells. The Alu editing index represents the combined A-to-I editing efficiency calculated from detected editing sites belonging to the same Alu element. **d**, HT-29 cells stably expressing wild-type ZBP1 (ZBP1^{WT}) or Zα domain mutant ZBP1 (ZBP1^{Zα1Zα2mut}) were transfected with 50 ng *NICN1* or *BPNT1* 3′ UTR Alu duplex RNA. **e**, Transfection of HT-29 ZBP1^{WT} with 50 ng of *NICN1* UTR duplex RNA in combination with 3 μM GSK′840 and/or 20 μM zVAD-FMK. Cell death in **d** and **e** was analysed as in Fig. 3d, and data are representative of three independent experiments. Fitted lines represent a logistic growth fit and data points show the mean and s.e.m.

Discussion

Collectively, we demonstrated that ADAR1 is a negative regulator of ZBP1-mediated apoptosis and necroptosis, which is in line with a recent study[41] showing that loss of ADAR1 sensitizes cells to ZBP1-induced death caused by nuclear export inhibition. The P193A mutation within the Zα domain of *ADAR1* causes AGS when paired with an ADAR-null allele[2]. Our study using *Adar*$^{Zα/-}$ mice, which mimic these compound heterozygous mutations, showed that ZBP1 may contribute to AGS pathology[7]. It is conceivable that bilateral striatal necrosis, a phenotype that specifically manifests in patients with AGS caused by *ADAR* mutations and involves an acute loss of neurons[42], is triggered by ZBP1-mediated cell death of neuronal cells. Finally, this study implicated ZBP1 as a sensor for endogenous Alu duplex RNA, along with recent studies showing

that ZBP1 acts as a dsRNA sensor during virus infection[43,44]. These findings further substantiate the concept that ZBP1 constitutes an integral part of the mammalian dsRNA response.

Online content

Any methods, additional references, Nature Research reporting summaries, source data, extended data, supplementary information, acknowledgements, peer review information; details of author contributions and competing interests; and statements of data and code availability are available at https://doi.org/10.1038/s41586-022-04974-w.

1. Samuel, C. E. Adenosine deaminase acting on RNA (ADAR1), a suppressor of double-stranded RNA-triggered innate immune responses. *J. Biol. Chem.* **294**, 1710–1720 (2019).
2. Rice, G. I. et al. Mutations in ADAR1 cause Aicardi–Goutieres syndrome associated with a type I interferon signature. *Nat. Genet.* **44**, 1243–1248 (2012).
3. Liddicoat, B. J. et al. RNA editing by ADAR1 prevents MDA5 sensing of endogenous dsRNA as nonself. *Science* **349**, 1115–1120 (2015).
4. Ward, S. V. et al. RNA editing enzyme adenosine deaminase is a restriction factor for controlling measles virus replication that also is required for embryogenesis. *Proc. Natl Acad. Sci. USA* **108**, 331–336 (2011).
5. Wang, Q. et al. Stress-induced apoptosis associated with null mutation of ADAR1 RNA editing deaminase gene. *J. Biol. Chem.* **279**, 4952–4961 (2004).
6. Hartner, J. C. et al. Liver disintegration in the mouse embryo caused by deficiency in the RNA-editing enzyme ADAR1. *J. Biol. Chem.* **279**, 4894–4902 (2004).
7. Maurano, M. et al. Protein kinase R and the integrated stress response drive immunopathology caused by mutations in the RNA deaminase ADAR1. *Immunity* **54**, 1948–1960.e5 (2021).
8. Nakahama, T. et al. Mutations in the adenosine deaminase *ADAR1* that prevent endogenous Z-RNA binding induce Aicardi–Goutieres-syndrome-like encephalopathy. *Immunity* **54**, 1976–1988.e7 (2021).
9. Tang, Q. et al. Adenosine-to-inosine editing of endogenous Z-form RNA by the deaminase ADAR1 prevents spontaneous MAVS-dependent type I interferon responses. *Immunity* **54**, 1961–1975.e5 (2021).
10. de Reuver, R. et al. ADAR1 interaction with Z-RNA promotes editing of endogenous double-stranded RNA and prevents MDA5-dependent immune activation. *Cell Rep.* **36**, 109500 (2021).
11. Guo, X. et al. Aicardi–Goutieres syndrome-associated mutation at *ADAR1* gene locus activates innate immune response in mouse brain. *J. Neuroinflammation* **18**, 169 (2021).
12. Inoue, M. et al. An Aicardi–Goutieres syndrome-causative point mutation in *Adar1* gene invokes multiorgan inflammation and late-onset encephalopathy in mice. *J. Immunol.* https://doi.org/10.4049/jimmunol.2100526 (2021).
13. Pestal, K. et al. Isoforms of RNA-editing enzyme ADAR1 independently control nucleic acid sensor MDA5-driven autoimmunity and multi-organ development. *Immunity* **43**, 933–944 (2015).
14. Mannion, N. M. et al. The RNA-editing enzyme ADAR1 controls innate immune responses to RNA. *Cell Rep.* **9**, 1482–1494 (2014).
15. Hartner, J. C., Walkley, C. R., Lu, J. & Orkin, S. H. ADAR1 is essential for the maintenance of hematopoiesis and suppression of interferon signaling. *Nat. Immunol.* **10**, 109–115 (2009).
16. Bajad, P. et al. An internal deletion of *ADAR* rescued by MAVS deficiency leads to a minute phenotype. *Nucleic Acids Res.* **48**, 3286–3303 (2020).
17. Placido, D., Brown, B. A. 2nd, Lowenhaupt, K., Rich, A. & Athanasiadis, A. A left-handed RNA double helix bound by the Zα domain of the RNA-editing enzyme ADAR1. *Structure* **15**, 395–404 (2007).
18. Schwartz, T., Rould, M. A., Lowenhaupt, K., Herbert, A. & Rich, A. Crystal structure of the Zα domain of the human editing enzyme ADAR1 bound to left-handed Z-DNA. *Science* **284**, 1841–1845 (1999).
19. Maelfait, J. et al. Sensing of viral and endogenous RNA by ZBP1/DAI induces necroptosis. *EMBO J.* **36**, 2529–2543 (2017).
20. Deigendesch, N., Koch-Nolte, F. & Rothenburg, S. ZBP1 subcellular localization and association with stress granules is controlled by its Z-DNA binding domains. *Nucleic Acids Res.* **34**, 5007–5020 (2006).
21. Feng, S. et al. Alternate rRNA secondary structures as regulators of translation. *Nat. Struct. Mol. Biol.* **18**, 169–176 (2011).
22. Devos, M. et al. Sensing of endogenous nucleic acids by ZBP1 induces keratinocyte necroptosis and skin inflammation. *J. Exp. Med.* **217**, e20191913 (2020).
23. Jiao, H. et al. Z-nucleic-acid sensing triggers ZBP1-dependent necroptosis and inflammation. *Nature* **580**, 391–395 (2020).
24. Wang, R. et al. Gut stem cell necroptosis by genome instability triggers bowel inflammation. *Nature* **580**, 386–390 (2020).
25. Kesavardhana, S. et al. The Zα2 domain of ZBP1 is a molecular switch regulating influenza-induced PANoptosis and perinatal lethality during development. *J. Biol. Chem.* **295**, 8325–8330 (2020).
26. Ingram, J. P. et al. ZBP1/DAI drives RIPK3-mediated cell death induced by IFNs in the absence of RIPK1. *J. Immunol.* **203**, 1348–1355 (2019).
27. Schwarzer, R., Jiao, H., Wachsmuth, L., Tresch, A. & Pasparakis, M. FADD and caspase-8 regulate gut homeostasis and inflammation by controlling MLKL- and GSDMD-mediated death of intestinal epithelial cells. *Immunity* **52**, 978–993.e6 (2020).
28. Vongpipatana, T., Nakahama, T., Shibuya, T., Kato, Y. & Kawahara, Y. ADAR1 regulates early T cell development via MDA5-dependent and -independent pathways. *J. Immunol.* **204**, 2156–2168 (2020).
29. Liddicoat, B. J. et al. Adenosine-to-inosine RNA editing by ADAR1 is essential for normal murine erythropoiesis. *Exp. Hematol.* **44**, 947–963 (2016).
30. Hur, S. Double-stranded RNA sensors and modulators in innate immunity. *Annu. Rev. Immunol.* **37**, 349–375 (2019).
31. Kim, J. I. et al. RNA editing at a limited number of sites is sufficient to prevent MDA5 activation in the mouse brain. *PLoS Genet.* **17**, e1009516 (2021).
32. Kuriakose, T. et al. ZBP1/DAI is an innate sensor of influenza virus triggering the NLRP3 inflammasome and programmed cell death pathways. *Sci. Immunol.* **1**, aag2045 (2016).
33. Thapa, R. J. et al. DAI senses influenza A virus genomic RNA and activates RIPK3-dependent cell death. *Cell Host Microbe* **20**, 674–681 (2016).
34. Kreuz, S., Siegmund, D., Scheurich, P. & Wajant, H. NF-κB inducers upregulate cFLIP, a cycloheximide-sensitive inhibitor of death receptor signaling. *Mol. Cell. Biol.* **21**, 3964–3973 (2001).
35. Micheau, O., Lens, S., Gaide, O., Alevizopoulos, K. & Tschopp, J. NF-κB signals induce the expression of c-FLIP. *Mol. Cell. Biol.* **21**, 5299–5305 (2001).
36. Dillon, C. P. et al. Survival function of the FADD–caspase-8–cFLIP$_L$ complex. *Cell Rep.* **1**, 401–407 (2012).
37. Oberst, A. et al. Catalytic activity of the caspase-8-FLIP$_L$ complex inhibits RIPK3-dependent necrosis. *Nature* **471**, 363–367 (2011).
38. Guo, H. et al. Species-independent contribution of ZBP1/DAI/DLM-1-triggered necroptosis in host defense against HSV1. *Cell Death Dis.* **9**, 816 (2018).
39. Ahmad, S. et al. Breaching self-tolerance to Alu duplex RNA underlies MDA5-mediated inflammation. *Cell* **172**, 797–810.e13 (2018).
40. Chung, H. et al. Human ADAR1 prevents endogenous RNA from triggering translational shutdown. *Cell* **172**, 811–824.e14 (2018).
41. Karki, R. et al. ADAR1 restricts ZBP1-mediated immune response and PANoptosis to promote tumorigenesis. *Cell Rep.* **37**, 109858 (2021).
42. Livingston, J. H. et al. A type I interferon signature identifies bilateral striatal necrosis due to mutations in *ADAR1*. *J. Med. Genet.* **51**, 76–82 (2014).
43. Koehler, H. et al. Vaccinia virus E3 prevents sensing of Z-RNA to block ZBP1-dependent necroptosis. *Cell Host Microbe* **29**, 1266–1276.e5 (2021).
44. Zhang, T. et al. Influenza virus Z-RNAs induce ZBP1-mediated necroptosis. *Cell* **180**, 1115–1129.e13 (2020).

Methods

Mice

Adar$^{+/-}$, *Adar*$^{Zα/Zα10}$ and *Zbp1*$^{Zα1α2/Zα1α2}$ mice[21] and were generated in C57BL/6 embryonic stem cells and have been previously described. *Mavs*$^{-/-}$ mice were obtained from J. Tschopp[45]. *Ripk3*$^{-/-}$ mice were obtained from V. Dixit[46]. *Mlkl*$^{-/-}$*Casp8*$^{-/-}$ mice were generated by crossing a *Mlkl*$^{fl/fl}$*Casp8*$^{fl/fl}$ male to a female *Sox2-cre* deleter mouse[47] to generate *Mlkl*$^{+/-}$*Casp8*$^{+/-}$ offspring. *Mlkl*$^{fl/fl}$ mice were obtained from J. Murphy[48] and *Casp8*$^{fl/fl}$ mice were obtained from S. Hedrick[49]. All alleles were maintained on a C57BL/6 genetic background. Allocation of groups was not random and determined by the genotype of the mice. Mice were age-matched but not sex-matched. Investigators were not blinded during data collection. Histological evaluation of TUNEL data presented in Figs. 1b,c, 2b,c, 3f,g and Extended Data Fig. 1e,f was performed blindly. Mice were housed in individually ventilated cages at the VIB-UGent Center for Inflammation Research in a specific pathogen-free facility according to national and institutional guidelines for animal care. Sequences of primers used for genotyping are listed in Supplementary Table 1. All experiments were conducted following approval by the local Ethics Committee of Ghent University.

Antibodies and reagents

Antibodies against the following proteins were used for western blot analysis: ADAR1 (14175, Cell Signaling Technology); ADAR1-p150 (293003, Synaptic Systems; A303-883A, Bethyl); RIPK1 (3493, Cell Signaling Technology); RIPK3 (2283, ProSci; 10188, Cell Signaling Technology); MLKL (MABC604, Millipore; GTX107538, GeneTex); p-MLKL (ab187091, Abcam; 37333, Cell Signaling Technology); ZBP1 (AG-20B-0010, Adipogen; 60968, Cell Signaling Technology); caspase-8 (8592, Cell Signaling Technology); TRIF (4596; Cell Signaling Technology); MAVS (4983, Cell Signaling Technology); and β-tubulin (ab21058, Abcam). Mouse anti-human caspase-8 antibody was provided by P. H. Krammer (German Cancer Research Center). The following secondary antibodies were used for detection: donkey anti-rabbit IgG–HRP (NA934, GE Healthcare); sheep anti-mouse IgG–HRP (NA931, GE Healthcare); and goat anti-rat IgG (NA935, GE Healthcare).

The following fluorochrome-conjugated antibodies and dyes were used for flow cytometry analysis: PE–cyanine5 CD19 (15-0193-82, Thermo Fisher Scientific); AlexaFluor 700 CD19 (56-0193-80, Thermo Fisher Scientific); BUV395 CD3e (563565, BD Biosciences); PE–Cy7 CD11c (25-0114-82, Thermo Fisher Scientific); FITC MHC class II (I-A/I-E) (11-5321-82, eBioscience); BV605 mouse anti-mouse CD161 (NK-1.1; 563220, BD Biosciences); PerCP–Cy5.5 rat anti-mouse CD11b (550993, BD Biosciences); APC-eFluor780 CD11b (47-0112-80, Thermo Fisher Scientific); BUV735 CD4 (564298, BD Biosciences); eFluor450 CD8a (48-0081-82, eBioscience); FITC CD8a (100705, BioLegend); PE XCR1 (148203, BioLegend); PerCP–eFluor710 CD172a (SIRP-α; 46-1721-82, eBioscience); BV785 Ly-6G (127645, BioLegend); APC–Cy7 Ly-6C (560596, BD Biosciences); BV711 CD64 (139311, BioLegend); AlexaFluor 700 CD45 (56-0451-80, Thermo Fisher Scientific); BV421 Siglec-F (565934, BD Biosciences); PE CD200R3 (142205, BioLegend); APC–Cy7 TCR β-chain (109220, BioLegend); APC F4/80 (17-4801, Thermo Fisher Scientific); PE–CF594 γδ TCR (563532, BD Biosciences); CD16/CD32 (Fc block; 553142, BD Biosciences); and eFluor506 FVD (65-0866-14, Thermo Fisher Scientific).

Mouse and human TNF, mouse IFNγ and mouse anti-TNF neutralizing antibodies (clone 1F3F3D4) were produced by the VIB protein Service Facility. IFNα-B/D (CGP35269, Novartis), human IFNα2 (592704, BioLegend), human IFNγ (300-02, PeproTech), zVAD-FMK (BACEN-1510.0005, Bachem), CHX (C7698, Sigma-Aldrich), BV6 (S7597, Selleckchem). HSV1-ICP6^{mutRHIM} was a gift from J. Han[50].

Cell culture

HT-29 cells (American Type Culture Collection (ATCC, HTB-38) were cultured at 37 °C and 5% CO_2 in McCoy's 5a medium (16600082, Gibco) supplemented with 10% FCS (TICO Europe), 2 mM glutamine (BE17-605F, Lonza) and 1 mM sodium pyruvate (S8636, Sigma-Aldrich). HEK293T cells (ATCC, CRL-3216) were cultured in high-glucose (4,500 mg l^{-1}) DMEM (41965–039, Gibco) supplemented with 10% FCS (TICO Europe) and 2 mM glutamine (BE17-605F, Lonza). *ADAR* Zα domain mutant HEK293 clones derived from the HEK293 cell line (CRL-1573, ATCC) were generated previously[10] and cultured at 37 °C and 5% CO_2 in DMEM/F-12 (31330-038, Gibco) supplemented with 10% FCS (TICO Europe), 2 mM glutamine (BE17-605F, Lonza) and 1 mM sodium pyruvate (S8636, Sigma-Aldrich). The cell lines were not authenticated. All cell lines tested negative for mycoplasma contamination.

For lentivirus production, HEK293T cells were transfected with C-terminal EGFP and V5-tagged wild-type human ZBP1 or Zα1α2 mutant human ZBP1 transducing vectors in the pDG2i backbone[51] together with the pCMV delta R8.91 gag-pol-expressing packaging plasmids and pMD2.G VSV-G-expressing envelope plasmid. After 24 h of transfection, the medium was refreshed. After 48 h of transfection, the virus supernatant was collected and used for transduction of 500,000 HT-29 cells seeded in 6-well plates in the presence of 8 μg ml^{-1} polybrene (H9268, Sigma-Aldrich). The next day, medium was refreshed and 2 days later, cells were seeded in a T75 flask in selection medium containing 2 μg ml^{-1} puromycin (P7255, Sigma-Aldrich). Transduced cells were sorted for EGFP expression on a FACSMelody cell sorter (BD Biosciences), and clones originating from single cells were established.

Primary lung fibroblasts were isolated from lungs of mice of the indicated genotypes. Lungs were sterilized with 70% ethanol before cutting the tissue into pieces of about 25 mm. Digestion was performed with 0.1% collagenase D (11088866001, Roche) and 0.2% trypsin solution (15090-046, Gibco) for 30 min at 37 °C. The collagenase D and trypsin solution was refreshed and digestion was continued for another 30 min at 37 °C. After neutralization with αMEM-20 (αMEM (22571-020, Gibco) supplemented with 20% FCS, 2 mM glutamine (BE17-605F, Lonza), 1 mM sodium pyruvate (S8636, Sigma-Aldrich), 100 U ml^{-1} penicillin and 100 μg ml^{-1} streptomycin (P4333, Sigma-Aldrich)), cells were pelleted at 400*g* for 5 min and resuspended in αMEM-20 culture medium. The purity of primary lung fibroblasts was assured by passaging each fibroblast line for at least three times in αMEM-20, which selectively supports the growth of fibroblasts, whereas other cell types die or stop proliferating. Primary mouse lung fibroblasts were maintained under hypoxic conditions (3% O_2 at 37 °C and 5% CO_2 in αMEM-20).

Western blotting

For western blotting, cells were washed twice with ice-cold PBS and lysed in protein lysis buffer (50 mM Tris-HCl pH 7.5 (15567027, Gibco), 1% IGEPAL CA-630 (I8896, Sigma-Aldrich), 150 mM NaCl and 10% glycerol (7122301, Biosolve) supplemented with complete protease inhibitor cocktail (11697498001, Roche) and PhosSTOP (4906845001, Roche). HT-29 cell lysates were cleared by centrifugation at 20,000*g* for 10 min. Embryonic tissue and primary mouse lung fibroblast lysates were cleared at 12,000*g* for 20 min. Laemmli loading buffer (5×; 250 mM Tris HCl, pH 6.8, 10% SDS, 0.5% bromophenol blue, 50% glycerol and 20% β-mercaptoethanol) was added to the supernatant. Finally, samples were incubated at 95 °C for 5 min and analysed using Tris-glycine SDS–PAGE and semi-dry immunoblotting.

RT–qPCR

For RT–qPCR, tissue was homogenized in TRIzol reagent (15596-018, Gibco) followed by phase separation with chloroform. Next, the aqueous layer was loaded onto Nucleospin RNA Plus columns (740984.250, Macherey-Nagel). cDNA synthesis was performed with a SensiFast cDNA synthesis kit (BIO-65054, Bioline). PrimeTime qPCR master mix (1055771, IDT) was used for cDNA amplification using a Lightcycler 480 system (Roche). The primers and probes (Taqman) used for RT–qPCR in this study are listed in Supplementary Table 1.

Histology

Intestinal tissues were fixed overnight at 4 °C in 10% formalin. Next, samples were embedded in paraffin and sectioned at 5 µm thickness. Haematoxylin and eosin (H&E) staining was performed using a Varistain slide stainer. H&E-stained sections were imaged with a Zeiss Axio Scan slide scanner and further analysed with Zeiss blue software. TUNEL staining was performed using a TMR Red in situ cell death detection kit (12156792910, Sigma-Aldrich). All sections were counterstained with DAPI (D21490, Thermo Fisher Scientific). For immunohistochemistry, sections were deparaffinized and rehydrated using a Varistain slide stainer. Antigen retrieval was performed by boiling sections at 95 °C for 10 min in antigen retrieval solution (H-3300-250, Vector). For immunofluorescence keratin 5 staining, slides were treated with 3% H_2O_2 in PBS for 10 min and 0.1 M $NaBH_4$ in PBS for 2 h at room temperature to reduce background fluorescence. After washing in 1× PBS, tissues were blocked in 1% BSA and 1% goat serum in PBS for 30 min at room temperature. Incubation with the primary antibody anti-keratin 5 (1:1,000, PRB-160P, Covance) was performed overnight at 4 °C. The next day, slides were washed in 1× PBS and incubated with goat anti-rabbit Dylight488 (1:1,000; 35552, Thermo Fisher Scientific) and DAPI (1:1,000; D1306, Life Technologies) for 30 min at room temperature. Images were acquired on a Zeiss LSM880 Fast AiryScan confocal microscope using ZEN software (Zeiss) and processed using Fiji (ImageJ). For cleaved caspase-8 staining, slides were treated with 3% H_2O_2 in methanol for 10 min following the antigen retrieval step. Next, slides were washed in 1× PBS and blocking was performed using 10% goat serum in 1× PBS for 30 min. Primary antibody incubation using anti-cleaved caspase-8 (1:500; 8592S, Cell Signaling Technology) was done overnight at 4 °C. Biotin goat anti-rabbit IgG (1:300; BA-1000-1.5, Vector) was used as the secondary antibody. Finally, slides were incubated for 30 min in reagent A and B as described for the Vectastain ELITE ABC kit (PK-6100, Vector) followed by detection using an ImmPACT DAB peroxidase (HRP) substrate kit (SK-4105, Vector). Haematoxylin counterstaining was performed using a Varistain slide stainer and mounted in xylene-based mounting medium. Images were acquired on a Zeiss Axio Scan slide scanner using ZEN software (Zeiss).

Cell death assays

Primary mouse lung fibroblasts were seeded in 48-well plates (35,000 cells per well) or 6-well plates (330,000 cells per well) 1 day before treatment. HT-29 cells were seeded at 30,000 cells per well in 96-well plates. On the day of the experiment, the cell-impermeable dye Sytox Green (1 µM, Thermo Fisher Scientific; S7020) was added to the culture medium together with the indicated stimuli. Sytox Green uptake was imaged with an IncuCyte ZOOM Live-Cell Analysis system (Sartorius) at 37 °C and 5% CO_2. The relative percentage of Sytox Green cells was determined by dividing the number of Sytox-Green-positive cells per image by the percentage of confluency (using phase-contrast images) at every time point.

Alu duplex RNA transfection

HT-29 cells were seeded in 24-well plates (130,000 cells per well) 1 day before transfection. The next day, medium was replaced with fresh medium containing Sytox Green and inhibitors. Cells were transfected with 50 ng Alu duplex RNA using Lipofectamine 2000 transfection reagent (11668027, InvitroGen). Cell death was analysed as described above. *NICN1* and *BPNT1* 3′ UTR Alu duplex RNA was provided by S. Hur[39]. Alu duplex RNAs were prepared by T7 in vitro transcription and PAGE purification as previously described[39,52]. Alu sequences are listed in Supplementary Table 1.

Knockdown experiments

RNA silencing experiments in HT-29 cells were performed by reverse transfection using DharmaFECT 1 transfection reagent (T-2001, Horizon Discovery). For live-cell imaging analysis, 90,000 cells were reverse-transfected at a 20 nM final siRNA concentration per well of a 24-well plate in medium containing the indicated stimuli or inhibitors and Sytox Green. Cell death was analysed as described above. The following siRNAs were used: ON-TARGETplus SMARTpool siRNAs (Horizon Discovery) directed against human *ADAR* (L-008630-00-0005); *ZBP1* (L-014650-00-0005); *RIPK1* (L-004445-00-0005); *RIPK3* (E-003534-00); *CASP8* (L-003466-00-0005); *TICAM1* (L-012833-00-0005); and non-targeting control (D-001810-01-05). siRNA directed against *ADAR1-p150* (ref. [53]) was custom made by Thermo Fisher Scientific (Silencer Select siRNA). Sense strand: 5′-GCCUCGCGGGCGCAAUGAATT-3′; guide strand: 5′-UUCAUUGCGCCCGCGAGGCAT-3′.

Spleen, peripheral blood and skin processing for flow cytometry

Spleens of 5-day-old *Adar*$^{-/-}$*Mavs*$^{-/-}$*Zbp1*$^{+/+}$, *Adar*$^{-/-}$*Mavs*$^{-/-}$*Zbp1*$^{+/Z\alpha1Z\alpha2}$ and *Zbp1*$^{Z\alpha1Z\alpha2/Z\alpha1Z\alpha2}$ mice and control littermates were collected in ice-cold PBS. Spleens were digested for 30 min at 37 °C in digestion buffer (RPMI-1640 supplemented with 0.5 mg ml^{-1} collagenase D (11088866001, Roche) and 10 mg ml^{-1} DNase I (1010459001, Roche)) with regular mixing. After neutralization with RPMI-1640 medium containing 2% FCS, erythrocytes were lysed with ACK lysing buffer (10-548E, Lonza) and filtered through a 70-mm cell strainer to obtain single-cell solutions. Peripheral blood was collected in EDTA-coated tubes (20.1288, Sarstedt) by tail vein bleeding. ACK lysing buffer (1 ml; Lonza; 10-548E) was mixed with 100 ml blood and incubated for 10 min at room temperature. Cells were washed two times with ice-cold PBS and were stained for flow cytometry analysis. Pieces of shaved mouse skin (±12 cm^2) were isolated from 21-day-old *Adar*$^{+/+}$*Ripk1*^{EKO} and *Adar*$^{+/Z\alpha}$*Ripk1*^{EKO} mice and control littermates. Subcutaneous fat and muscle were removed by mechanical scraping with a scalpel. Subsequently, the skin was carefully placed in 0.4 mg ml^{-1} dispase II (4492078001, Roche) with the dermal side facing down for 2 h at 37 °C. Epidermis was separated from the dermis with a forceps, cut into fine pieces and incubated in 2 ml enzymatic solution containing 1.5 mg ml^{-1} collagenase type IV (LS004188, Worthington) and 0.5 mg ml^{-1} Dnase I (10104159001, Roche) for 20 min at 37 °C with shaking. After neutralization with 2% FCS RPMI medium, the cell suspension was filtered through a 70-µm cell strainer to obtain a single-cell suspension.

Flow cytometry

Single-cell suspensions were first stained with anti-mouse CD16/CD32 (Fc block; 553142, BD Biosciences) and dead cells were excluded with Fixable Viability Dye eFluor506 (65-0866-14, Thermo Fisher Scientific) for 30 min at 4 °C in PBS. Next, cell surface markers were stained for 30 min at 4 °C in FACS buffer (PBS, 5% FCS, 1 mM EDTA and 0.05% sodium azide). Cells were sorted on a LSR Fortessa or a FACSymphony (BD Biosciences). Data were analysed with FlowJo software (Tree Star). The total number of cells was counted on a FACSVerse (BD Biosciences).

Blood analysis

Peripheral blood was collected in EDTA-coated tubes by decapitation of 5-day-old pups. The total number of leukocytes, erythrocytes and whole-blood parameters were determined using a HEMAVET 950LV (Drew Scientific).

Sanger sequencing

cDNA from brain and spleen tissue derived from mice of the indicated genotypes was PCR-amplified using primers targeting the mRNA of *Htr2c* (forward: 5′-GGCCAGCACTTTCAATAGTCGTG-3′, reverse: 5′-CAATCTTCATGATGGCCTTAGTCC-3′), *Mad2l1* (forward: 5′-AATTTTCCGGTGAAGAAAGC-3′, reverse: 5′-AGCTTTGATC CCTTCTGCTG-3′) and *Rpa1* (forward: 5′-CTCAGAGGGCTG TGTGTGAA-3, reverse: 5′-AGACAAAAAGGTGCCACCAC-3′). The obtained PCR product was purified using a NucleoSpin Gel and PCR Clean-up kit (740609250, Macherey-Nagel) and sent for

Sanger sequencing with the forward primers or in the case of *Htr2c*: 5′-GGCGAATTCCATTGCTGATATGCTGGTG-3′.

RNA sequencing library preparation

Total RNA of IFNα2-treated HEK293 cells or untreated and hybrid IFNα-B/D-treated primary mouse lung fibroblasts was purified using RNeasy columns (Qiagen) with on-column DNase I digestion. RNA integrity was tested using an Agilent RNA 6000 Pico kit (Agilent; 50671513). Sequencing libraries were prepared using a Stranded mRNA ligation kit (Illumina) with the Ribo-Zero Gold kit (Illumina) for ribosomal depletion. Deep sequencing of the libraries was performed on an Illumina Novaseq6000, generating 150 bp paired-end sequencing reads.

A-to-I editing data analysis

To enable reproducible analysis from raw RNA sequencing data to the prediction of A-to-I editing sites by RDDpred[54], a Nextflow[55] pipeline was developed based on the RNA sequencing pipeline from the nf-core community[56]. To align with our previous A-to-I data analysis[10], the original nf-core trimming module was replaced by Trimmomatic[57], the editing site prediction tool RDDpred was inserted and a docker image was created (https://github.com/vibbits/RDDpred). For the mapping of the mouse and human samples using STAR 2.7.3a, the reference genomes mm10 and hg19, respectively, were used. Positive machine-learning training sets for RDDpred consisted of annotated A-to-I editing sites derived from the DARNED[58], RADAR[59] and REDIportal[60] databases. The negative training set consisted of mapping error-prone sites observed following mapping to the hg19 and mm10 genomes (http://epigenomics.snu.ac.kr/RDDpred/prior.php). The entire pipeline with references to the genome and STAR indices is available on GitHub (https://github.com/vibbits/rnaseq-editing). This pre-processing pipeline was executed on the human and mice samples using Azure Kubernetes services. The raw output of RDDpred was further analysed by assigning strand topology to each identified RNA–DNA difference (RDD). To this end, BAM files were split in half samples containing reads that were either mapped to the sense or antisense strand. Next, quantification of total read coverage and variant read frequency was performed for all detected A>G and T>C RDDs in each half sample using Bam-readcount (https://github.com/genome/bam-readcount). Ambiguous RDDs (for example, multiple variant calls per site, RDDs detected on both strands), RDDs (murine dataset) overlapping with annotated C57BL/6-specific SNPs (Sanger Institute Mouse Genomes project v.3; dbSNPv137) or (human dataset) HEK293-specific SNPs (http://hek293genome.org/v2/data.php; data trackCG293, converted to hg19 assembly using LiftOver) and RDDs that were also detected in ADAR1-deficient cells were removed from the datasets. Finally, identified editing sites with a read coverage below ten or were observed in fewer than three different samples (independent of genotype) were excluded from the final datasets. Next, the repeat element status of each editing site was determined based on the RepeatMasker annotation (www.repeatmasker.org; Repeat Library 20140131) and the repeat/Alu editing index was calculated by dividing the combined number of detected variants (A>G or T>C) by the combined total number of reads covering the A-to-I editing sites identified in a single repeat element. Repeat/Alu elements of which editing activity was restricted to a single genotype were reported when editing was observed in all samples of that genotype. For differential editing analysis, only repeat/Alu elements that displayed editing in all three wild-type and all three mutant samples were included. Differentially edited repeats/Alu elements (P value < 0.05) were determined by Welch two Sample t-test on the $\log_{10}$ values of the calculated editing index. See Supplementary Table 2 for a list of differentially edited repeat/Alu elements. In silico RNA folding analysis was performed using the RNAfold webtool from the Vienna RNA Websuite[61] using the default parameters and the algorithm 'minimum free energy (MFE) and partition function'. The change in folding characteristics due to A-to-I editing was calculated by introducing constraints that mimic the complete lack of base pairing on the identified A-to-I editing sites.

Statistical analysis

Statistical analyses were performed in Prism 8.3.0 (GraphPad Software). Statistical methods are described in the figure legends.

Reporting summary

Further information on research design is available in the Nature Research Reporting Summary linked to this paper.

Data availability

Raw RNA sequencing data used in this study are available from the European Nucleotide Archive (https://www.ebi.ac.uk/ena/browser/home) with accession codes PRJEB52610 (mouse primary lung fibroblasts) and PRJEB52618 (HEK293 cells). Source data are provided with this paper.

Code availability

The complete pipeline used for the A-to-I editing analysis from raw RNA sequencing data to the original output of the editing site prediction tool RDDpred with references to the genome and STAR indices is made available on GitHub (https://github.com/vibbits/rnaseq-editing). Any additional information required to reanalyse the data reported in this paper is available from the lead contact upon request.

45. Michallet, M. C. et al. TRADD protein is an essential component of the RIG-like helicase antiviral pathway. *Immunity* **28**, 651–661 (2008).
46. Newton, K., Sun, X. & Dixit, V. M. Kinase RIP3 is dispensable for normal NF-κBs, signaling by the B-cell and T-cell receptors, tumor necrosis factor receptor 1, and Toll-like receptors 2 and 4. *Mol. Cell. Biol.* **24**, 1464–1469 (2004).
47. Hayashi, S., Lewis, P., Pevny, L. & McMahon, A. P. Efficient gene modulation in mouse epiblast using a *Sox2Cre* transgenic mouse strain. *Mech. Dev.* **119**, S97–S101 (2002).
48. Murphy, J. M. et al. The pseudokinase MLKL mediates necroptosis via a molecular switch mechanism. *Immunity* **39**, 443–453 (2013).
49. Beisner, D. R., Ch'en, I. L., Kolla, R. V., Hoffmann, A. & Hedrick, S. M. Cutting edge: innate immunity conferred by B cells is regulated by caspase-8. *J. Immunol.* **175**, 3469–3473 (2005).
50. Huang, Z. et al. RIP1/RIP3 binding to HSV-1 ICP6 initiates necroptosis to restrict virus propagation in mice. *Cell Host Microbe* **17**, 229–242 (2015).
51. De Groote, P. et al. Generation of a new Gateway-compatible inducible lentiviral vector platform allowing easy derivation of co-transduced cells. *Biotechniques* **60**, 252–259 (2016).
52. Peisley, A. et al. Cooperative assembly and dynamic disassembly of MDA5 filaments for viral dsRNA recognition. *Proc. Natl Acad. Sci. USA* **108**, 21010–21015 (2011).
53. Sakurai, M. et al. ADAR1 controls apoptosis of stressed cells by inhibiting Staufen1-mediated mRNA decay. *Nat. Struct. Mol. Biol.* **24**, 534–543 (2017).
54. Kim, M. S., Hur, B. & Kim, S. RDDpred: a condition-specific RNA-editing prediction model from RNA-seq data. *BMC Genomics* **17**, 5 (2016).
55. Di Tommaso, P. et al. Nextflow enables reproducible computational workflows. *Nat. Biotechnol.* **35**, 316–319 (2017).
56. Ewels, P. A. et al. The nf-core framework for community-curated bioinformatics pipelines. *Nat. Biotechnol.* **38**, 276–278 (2020).
57. Bolger, A. M., Lohse, M. & Usadel, B. Trimmomatic: a flexible trimmer for Illumina sequence data. *Bioinformatics* **30**, 2114–2120 (2014).
58. Kiran, A. M., O'Mahony, J. J., Sanjeev, K. & Baranov, P. V. Darned in 2013: inclusion of model organisms and linking with Wikipedia. *Nucleic Acids Res.* **41**, D258–D261 (2013).
59. Ramaswami, G. & Li, J. B. RADAR: a rigorously annotated database of A-to-I RNA editing. *Nucleic Acids Res.* **42**, D109–D113 (2014).
60. Mansi, L. et al. REDIportal: millions of novel A-to-I RNA editing events from thousands of RNAseq experiments. *Nucleic Acids Res.* **49**, D1012–D1019 (2021).
61. Lorenz, R. et al. ViennaRNA Package 2.0. *Algorithms Mol. Biol.* **6**, 26 (2011).

Acknowledgements We are grateful to the VIB-UGent IRC Animal house for mouse husbandry, and the VIB Flow and Bioimaging Cores for training, support and access to the instrument park. Research in the J.M. group was supported by an Odysseus II Grant (G0H8618N), EOS INFLADIS (40007512), a junior research grant (G031022N) from the Research Foundation Flanders (FWO), a CRIG young investigator proof-of-concept grant and by Ghent University. Research in the P.V. group was supported by EOS MODEL-IDI (30826052), EOS INFLADIS (40007512), FWO senior research grants (G.0C76.18N, G.0B71.18N, G.0B96.20N and G.0A9322N), Methusalem (BOF16/MET_V/007), iBOF20/IBF/039 ATLANTIS, the Foundation against Cancer (F/2016/865, F/2020/1505), CRIG and GIGG consortia, and VIB. Research in the S.H. group was supported by NIH grants R01AI154653 and R01AI111784. R.d.R. was supported by a Ghent University BOF PhD fellowship. S.V. and J.N. were supported by FWO PhD fellowships.

Author contributions R.d.R., S.V. and J.M. conceived the study. R.d.R., S.V., E.D., J.N. and J.M. designed, performed and analysed experiments and interpreted data. E.H., M.J. and G.B. performed and analysed experiments. F.V.N., L.V., G.v.L. and W.D. helped with experimental design. R.d.R. and A.B. performed bioinformatical analyses. S.A. and S.H. generated the Alu–Alu hybrids. J.M. supervised the experiments. R.d.R., S.V., P.V. and J.M. wrote the manuscript.

Competing interests The authors declare no competing interests.

Additional information

Supplementary information The online version contains supplementary material available at https://doi.org/10.1038/s41586-022-04974-w.

Correspondence and requests for materials should be addressed to Jonathan Maelfait.

Peer review information *Nature* thanks Andreas Linkermann, Seamus Martin and the other, anonymous, reviewer(s) for their contribution to the peer review of this work. Peer reviewer reports are available.

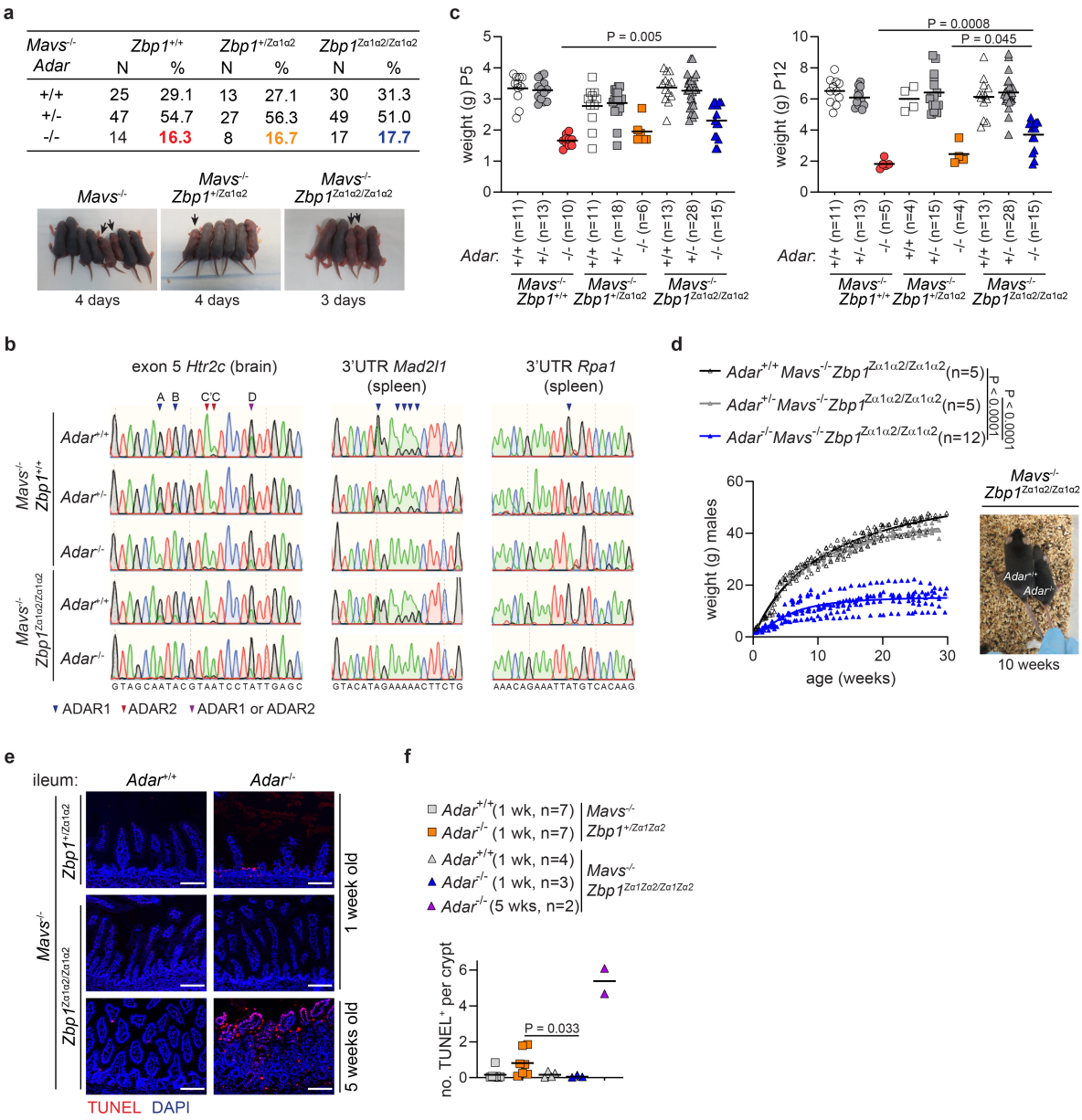

Extended Data Fig. 1 | Characterisation of *Adar*$^{-/-}$ *Mavs*$^{-/-}$ *Zbp1*$^{Zα1α2/Zα1α2}$ mice. a, Numbers and percentages of pups obtained from *Adar*$^{+/-}$ *Mavs*$^{-/-}$ *Zbp1*$^{+/+,+/Zα1α2 or Zα1α2/Zα1α2}$ breeding pairs. Lower panels show representative images of 3 or 4 day old pups. Arrows indicate *Adar/Mavs* double knockout mice with the indicated *Zbp1* genotypes. **b**, Sanger sequencing chromatograms of A-to-I editing sites in brain (*Htr2c*) or spleen (*Mad2l1* and *Rpa1*) tissues derived from mice of the indicated genotypes. ADAR1-, ADAR2- and ADAR1/ADAR2-specific sites indicated by blue, red and purple triangles, respectively. **c**, Weight in grams (g) of 5 (P5) or 12 (P12) day old mice of the indicated genotypes. **d**, Weight in grams (g) of male mice of the indicated genotypes measured weekly from birth till 30 weeks of age. Right panel shows a representative picture of a 10 week old *Adar*$^{-/-}$ *Mavs*$^{-/-}$ *Zbp1*$^{Zα1α2/Zα1α2}$ mouse and an *Adar*$^{+/+}$ *Mavs*$^{-/-}$ *Zbp1*$^{Zα1α2/Zα1α2}$ littermate. **e**, TUNEL assay on ileum sections from 1 week or 5 week old *Adar*$^{-/-}$ *Mavs*$^{-/-}$ mice expressing Zα domain mutant ZBP1 from one (*Zbp1*$^{+/Zα1α2}$) or two (*Zbp1*$^{Zα1α2/Zα1α2}$) alleles. Scale bar = 100 µm. **f**, quantification of TUNEL^{+} cells per crypt. Each data point in **(c,d,f)** represents an individual mouse. The numbers of mice (n) that were analysed per genotype in **(c,d,f)** are indicated in the graph. Lines in **(c,f)** represent the mean; P values by Mann-Whitney test. Lines in **(d)** represent a sigmoidal, 4PL fit; P values by two-way ANOVA.

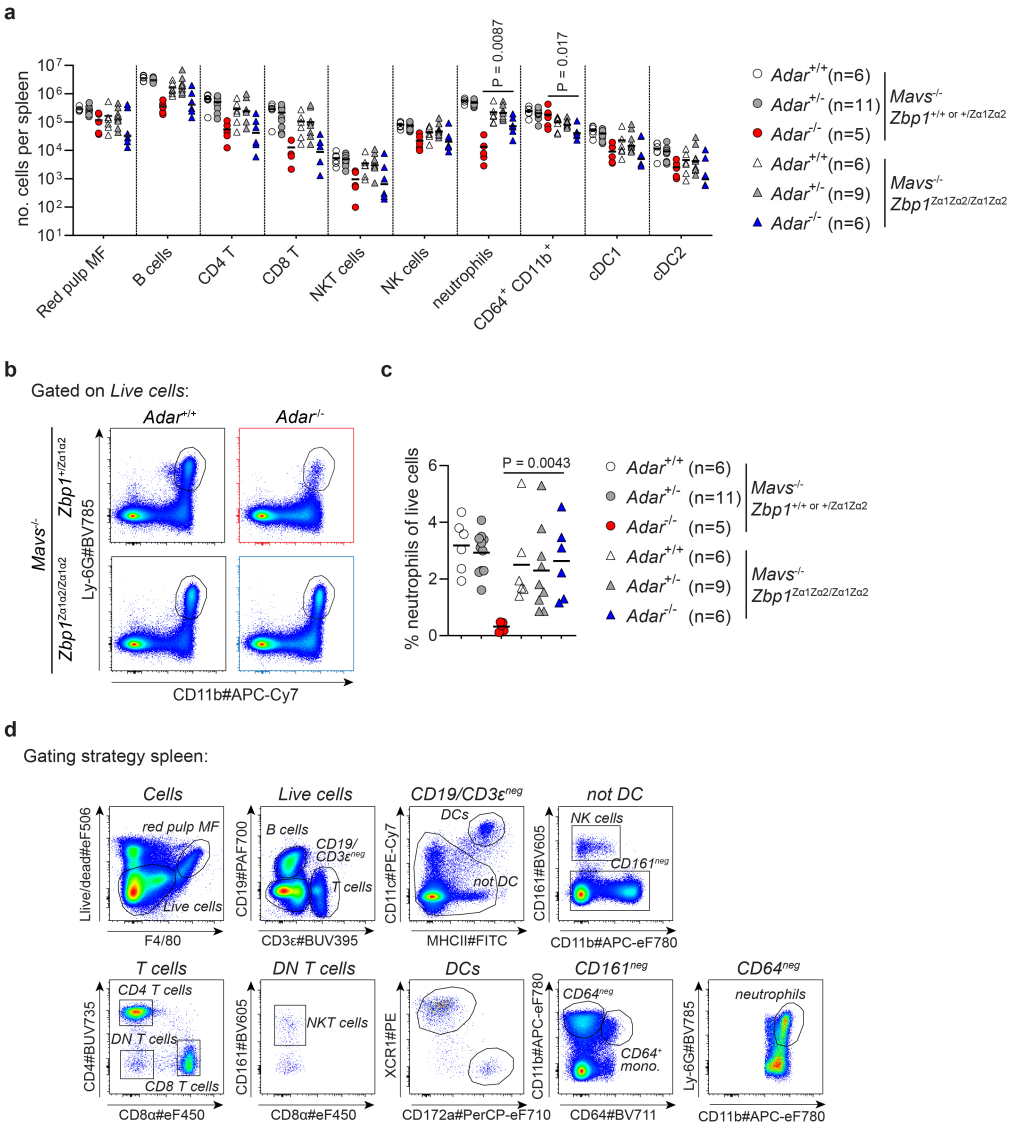

Extended Data Fig. 2 | Immune phenotyping of *Adar*$^{-/-}$ *Mavs*$^{-/-}$ *Zbp1*$^{Zα1α2/Zα1α2}$ mice. a, Flow cytometric quantification of numbers of immune cell populations in spleens of 4 to 5 day old *Adar*$^{-/-}$ *Mavs*$^{-/-}$ mice expressing wild-type (*Zbp1*$^{+/+,+/Zα1Zα2}$) or Zα domain mutant ZBP1 (*Zbp1*$^{Zα1α2/Zα1α2}$). **b**, Representative flow plots showing the presence of neutrophils in live cell populations in spleens of mice of the indicated genotypes. **c**, Percentage of neutrophils in the population of live cells in spleens. **d**, Flow cytometry gating strategy of immune cell populations in spleens shown in **(a,b)**. Lines in **(a,c)** represent the mean; each data point represents an individual mouse; the numbers of mice (n) that were analysed per genotype are indicated in the graph; P values by Mann-Whitney test.

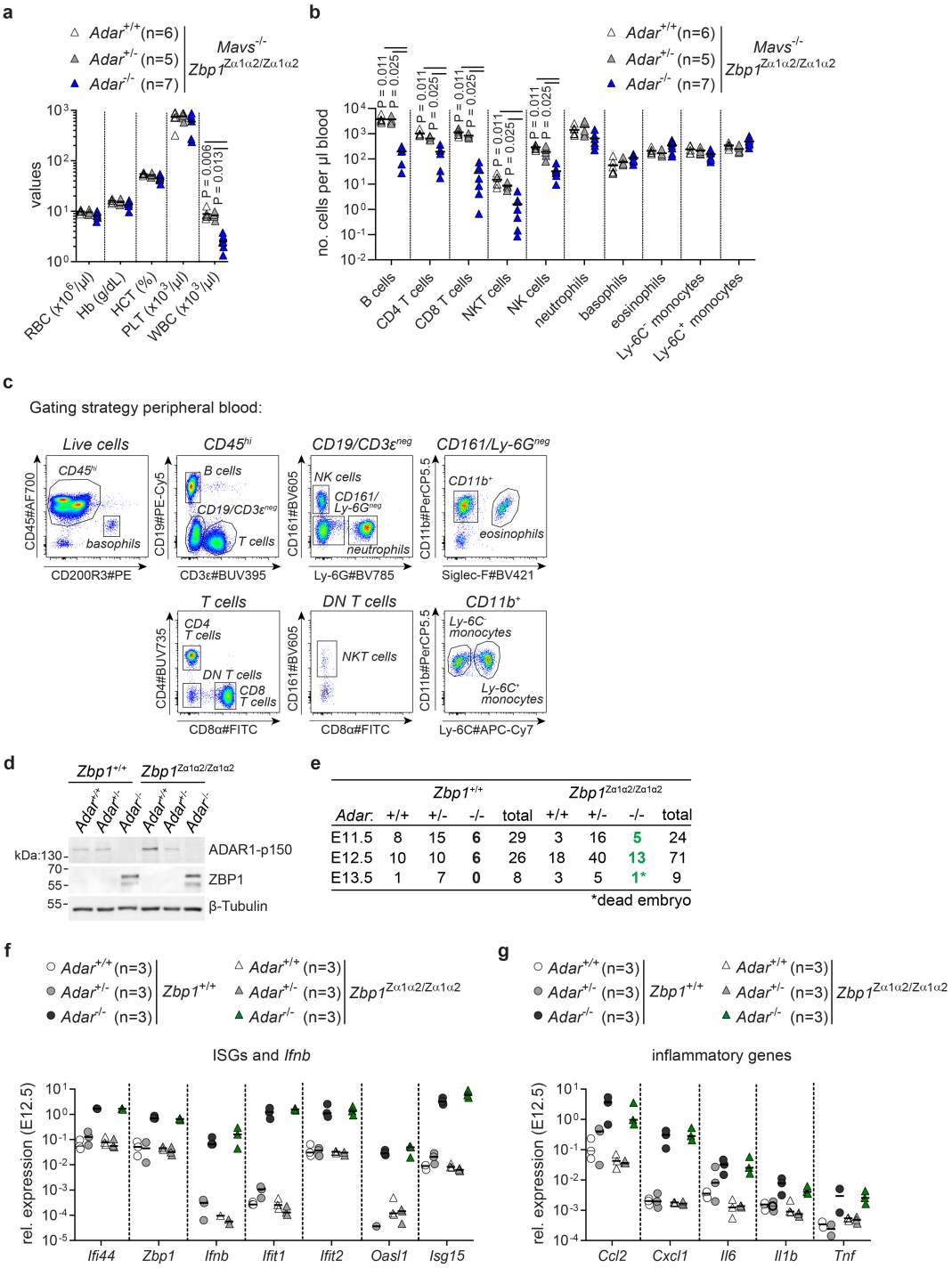

Extended Data Fig. 3 | Immune phenotyping of surviving *Adar*$^{-/-}$ *Mavs*$^{-/-}$ *Zbp1*$^{Zα1α2/Zα1α2}$ mice and analysis of *Adar*$^{-/-}$ *Zbp1*$^{Zα1α2/Zα1α2}$ embryos. **a**, Peripheral blood of 20 week old *Adar*$^{-/-}$ *Mavs*$^{-/-}$ *Zbp1*$^{Zα1α2/Zα1α2}$ pups and their littermates was analysed for total red blood cell (RBC), white blood cell (WBC) and platelet (PLT) numbers, together with haemoglobin (Hb) and haematocrit (HCT) levels. **b**, Flow cytometric quantification of numbers of circulating lymphocytes (B cells, CD4 and CD8 T cells, and NK and NKT cells) or myeloid cells (neutrophils, basophils, eosinophils and Ly-6C$^-$ and Ly-6C$^+$ monocytes) per µL of blood. **c**, Gating strategy for flow cytometry analysis in **(b)**. **d**, Immunoblot analysis of embryonic (E) day 12.5 whole embryo lysates of the indicated genotypes. **e**, Numbers of embryos resulting from interbreeding of *Adar*$^{+/-}$ *Zbp1*$^{+/+ \text{ or } Zα1α2/Zα1α2}$ breeding pairs and dissected on the indicated embryonic (E) days. **f,g**, RT-qPCR analysis of the indicated ISGs and *Ifnb* **(f)** or inflammatory genes **(g)** analysed in E12.5 embryos of the indicated genotypes. Lines in (**a**,**b**,**f**,**g**) represent the mean; each data point represents an individual mouse; each data point represents an individual mouse; the numbers of mice (n) that were analysed per genotype are indicated in the graph; P values by Mann-Whitney test. For gel source data, see Supplementary Figure 1.

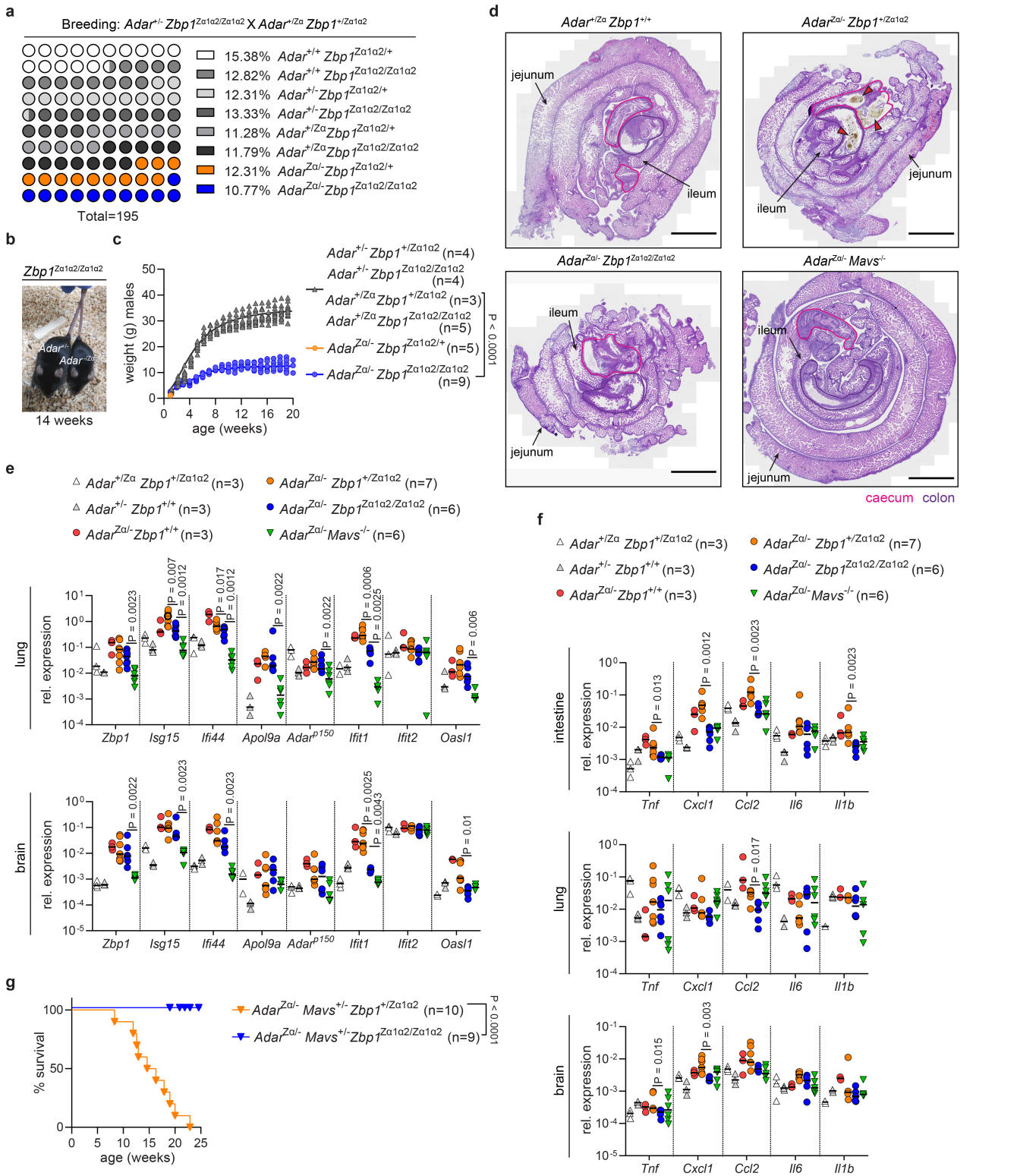

Extended Data Fig. 4 | Characterisation of *Adar*$^{Zα/-}$ *Zbp1*$^{Zα1α2/Zα1α2}$ and *Adar*$^{Zα/-}$ *Mavs*$^{+/-}$ *Zbp1*$^{Zα1α2/Zα1α2}$ mice. a, Percentages of offspring (n = 195) with the indicated genotypes obtained from *Adar*$^{+/-}$ *Zbp1*$^{Zα1α2/Zα1α2}$ X *Adar*$^{+/Zα}$ *Zbp1*$^{+/Zα1α2}$ breeding pairs. **b**, Representative image of a 14 week old *Adar*$^{Zα/-}$ *Zbp1*$^{Zα1α2/Zα1α2}$ mouse and its *Adar*$^{+/-}$ *Zbp1*$^{Zα1α2/Zα1α2}$ littermate. **c**, Weight in grams (g) of male mice of the indicated genotypes measured weekly from birth till 20 weeks of age. Each data point represents an individual mouse; lines represent a sigmoidal, 4PL fit; P value by two-way ANOVA. **d**, H&E staining of longitudinal sections of whole intestines from 1 day old mice from the indicated genotypes. Jejunum and ileum are indicated by arrows. Caecum and colon are indicated by a pink and purple line, respectively. Scale bar = 0.2 cm. Red triangles indicate necrotic tissue in caecum and colon. **e**, RT-qPCR analysis of the indicated ISGs, analysed in whole tissue lysates of lungs and brains of 1 day old pups of the indicated genotypes. **f**, RT-qPCR analysis of the indicated inflammatory genes, analysed in whole tissue lysates of intestines, lungs and brains of 1 day old pups of the indicated genotypes. Lines in **(e, f)** represent the mean; each data point represents an individual mouse; P values by Mann-Whitney test. **g**, Kaplan-Meier survival curve of mice from the indicated genotypes. P value by log-rank test. Numbers of mice (n) that were analysed per genotype in **(c,e,f,g)** are indicated in the graph.

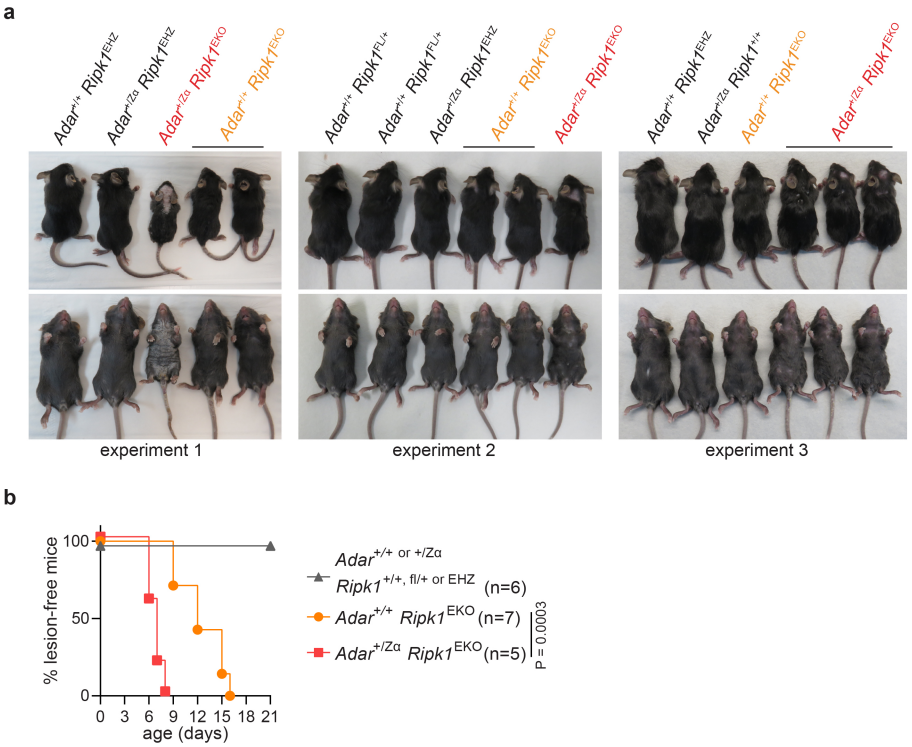

Extended Data Fig. 5 | *Adar*$^{+/Zα}$ *Ripk1*^{EKO} mice develop severe skin inflammation. a, Macroscopic images of 21 day old *Adar*$^{+/+}$ *Ripk1*^{EKO} mice, *Adar*$^{+/Zα}$ *Ripk1*^{EKO} mice and control littermates from 3 experiments. **b**, Kaplan-Meier plot of macroscopically visible lesion appearance of epidermis-specific RIPK1 knockout mice (*Ripk1*^{EKO}) carrying heterozygous ADAR1 Zα domain mutant alleles (*Adar*$^{+/Zα}$) or expressing wild type ADAR1. Littermate offspring containing two or one wild type *Ripk1* alleles (*Ripk1*$^{+/+,fl/+}$) or heterozygously expressing a functional *Ripk1* allele in the epidermis (*Ripk1*^{EHZ}) did not develop lesions and are shown as controls. Numbers of mice (n) that were analysed per genotype are indicated in the graph. P value by log-rank test.

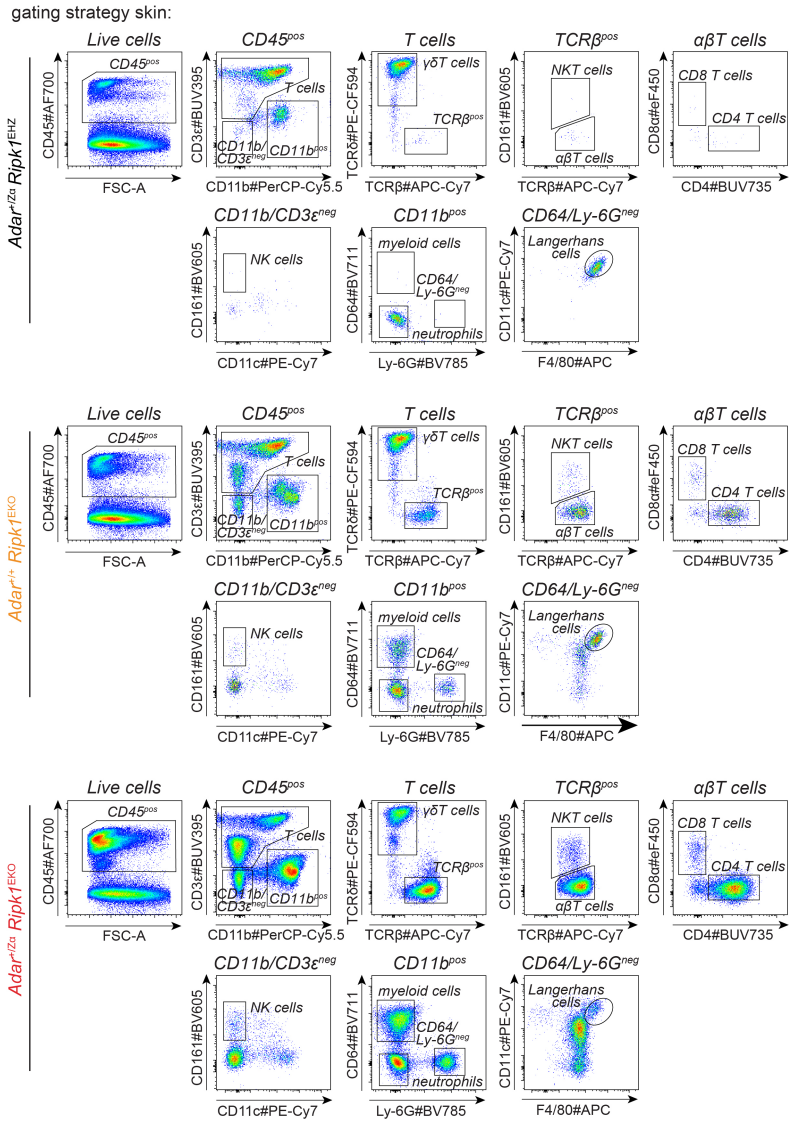

Extended Data Fig. 6 | Flow cytometry gating strategy of CD45$^+$ immune cell subsets in the skin. Representative flow plots of the immune cell subsets of the indicated genotypes are shown. The data are shown quantified in Fig. 2g.

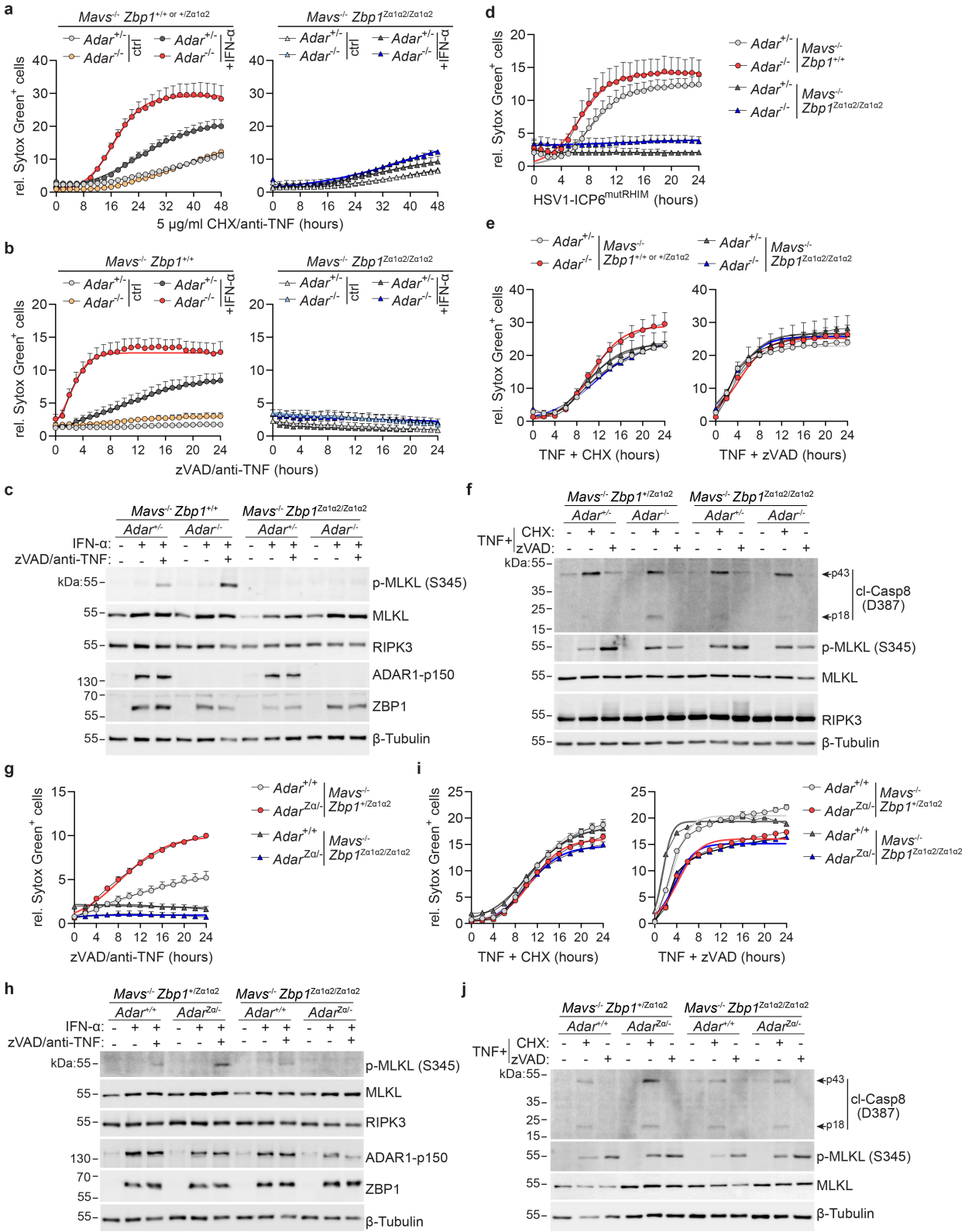

Extended Data Fig. 7 | ADAR1 deletion or Zα domain mutation induces ZBP1-mediated cell death of mouse fibroblasts. a-j, Primary mouse lung fibroblasts isolated from mice of the indicated genotypes were stimulated with 200 U/mL IFN-α **(a-c, e-j)** or 200 U/mL IFN-γ **(d)** for 16 h or left untreated (ctrl). Next, cells were treated with 5 μg/mL CHX and 1 μg/mL anti-mouse TNF **(a)**, 50 μM zVAD-fmk and 1 μg/mL anti-mouse TNF **(b,c,g,h)**, 30 ng/mL mouse TNF and 10 μg/mL CHX or 50 μM zVAD-fmk **(e,f,i,j)** or infected with HSV1 ICP6^{mutRHIM} at a multiplicity of infection of 5 **(d)**. Cell death in **(a,b,d,e,g,i)** was quantified by measuring relative (rel.) SYTOX Green uptake every 2 h. **c**, Immunoblot related to **(b)**. Samples were harvested 4 h post treatment. **f,j** Immunoblot related to **(e,i)**. Samples were harvested 7 (TNF + CHX) and 3 (TNF + zVAD) hours, respectively. **h**, Immunoblot related to **(g)**. Samples were harvested 8 h post treatment. Data points in **(a,b,d,e,g,i)** show the mean of 2-6 technical replicates (see Source Data) + SD and are representative of 3 independent experiments. Fitted lines represent a logistic growth fit. For gel source data, see Supplementary Figure 1.

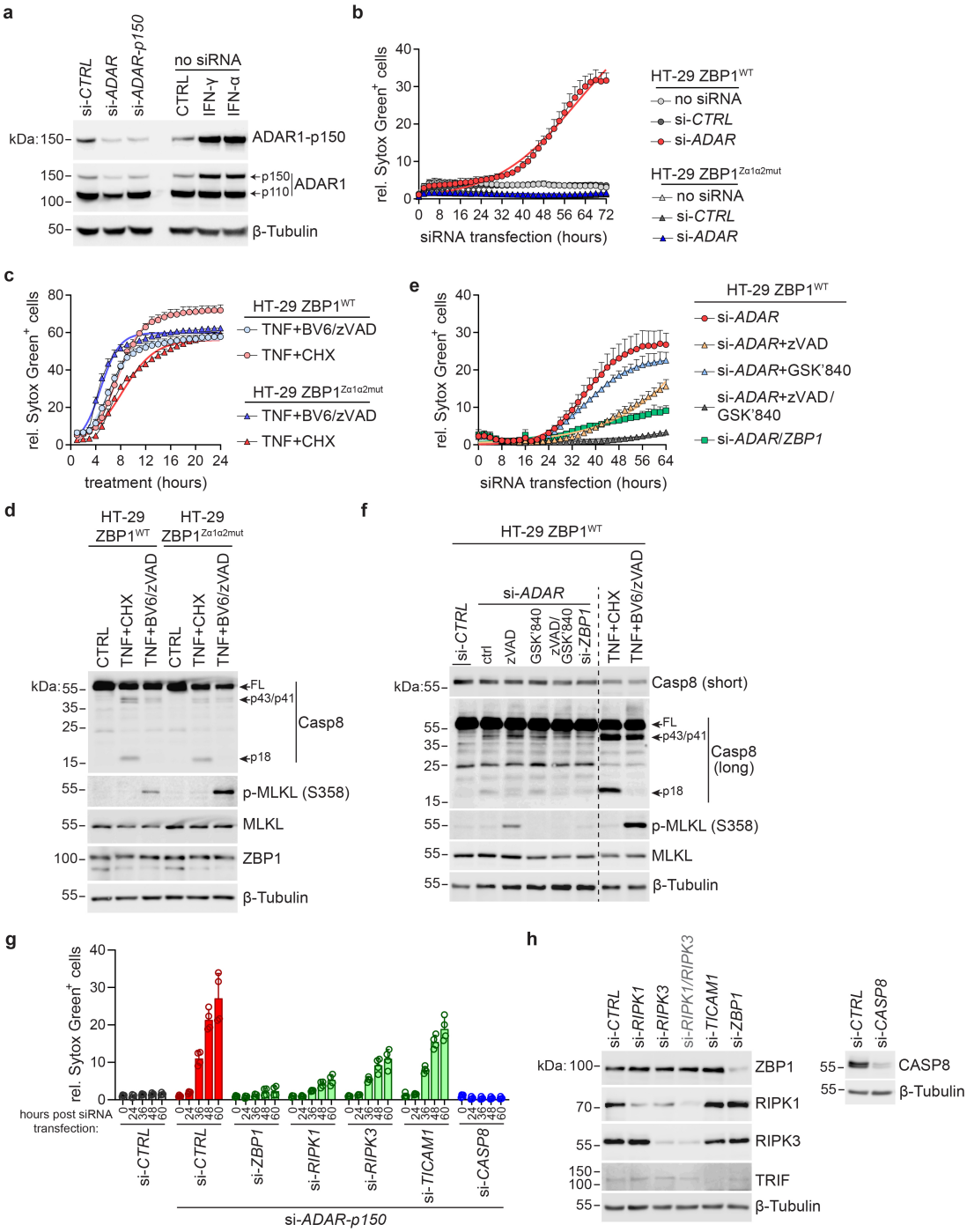

Extended Data Fig. 8 | ADAR1 depletion causes ZBP1-dependent cell death of human HT-29 cells. a, Immunoblot of HT-29 cells 48 h post transfection with non-targeting control siRNAs (si-*CTRL*), siRNAs targeting *ADAR* (si-*ADAR*) or the p150 isoform of *ADAR* (si-*ADAR-p150*). As controls, cells were treated with 1,000 U/mL IFN-α or 100 ng/mL IFN-γ. **b**, HT-29 cells stably expressing wild type ZBP1 (ZBP1^{WT}) or Zα domain mutant ZBP1 (ZBP1^{Zα1Zα2mut}) were transfected with non-targeting control siRNAs (si-*CTRL*) or siRNAs targeting *ADAR* (si-*ADAR*). Cell death was quantified by measuring relative (rel.) SYTOX Green uptake every 2 h. **c**, HT-29 ZBP1^{WT} and ZBP1^{Zα1Zα2mut} cells were treated with 30 ng/mL human TNF, 5 μM BV6 and 20 μM zVAD-fmk (TNF + BV6/ZVAD) or 30 ng/mL TNF and 20 μg/mL CHX (TNF + CHX). Cell death was quantified as in **(b)**. **d**, Immunoblot related to **(c)**. Cells were harvested 3 (TNF + BV6/ZVAD) or 6 (TNF+CHX) hours post treatment. FL, full length. **e**, HT-29 ZBP1^{WT} cells were transfected with si-*ADAR* only or si-*ADAR* and si-*ZBP1*. After five hours, cells were treated with 20 μM zVAD-fmk and/or 3 μM GSK'840 or left untreated. Cell death was analysed as in **(b)**. **f**, Immunoblot related to **(e)**. Samples were harvested 30 h post transfection. TNF + CHX and TNF + BV6/ZVAD control samples were treated and harvested as in **(d)**. **g**, HT-29 ZBP1^{WT} cells were transfected with si-*CTRL* or si-*ADAR-p150*. si-*ADAR-p150* was combined with si-*ZBP1*, or siRNAs targeting *RIPK1* (si-*RIPK1*), *RIPK3* (si-*RIPK3*), *TICAM1* (TRIF; si-*TICAM1*) or *CASP8* (si-*CASP8*). Cell death was quantified as in **(b)**. **h**, HT-29 ZBP1^{WT} cells transfected with the indicated siRNAs were harvested at 48 h post transfection for protein expression analysis. Fitted lines in **(b,c,e)** represent a logistic growth fit; Data points show mean of 3 **(b,c,e)** or 4 **(g)** technical replicates + SD and are representative of 3 independent experiments. For gel source data, see Supplementary Figure 1.

a

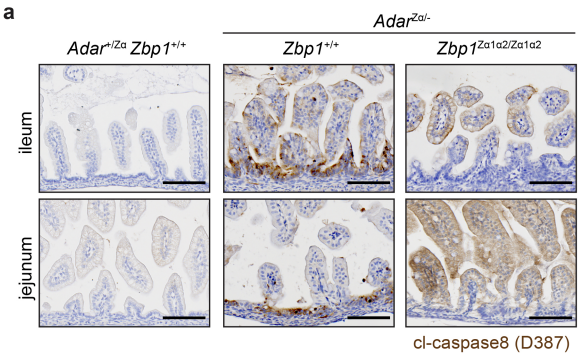

b

Breeding: *Adar*$^{+/-}$ *Ripk3*$^{+/-}$ X *Adar*$^{+/Zα}$ *Ripk3*$^{+/-}$

Adar	*Ripk3*	n	obs.%	exp.%
+/+	+/+	13	6.25	6.25
+/+	+/-	27	13.0	12.5
+/+	-/-	27	8.17	6.25
+/-	+/+	11	5.29	6.25
+/-	+/-	37	17.8	12.5
+/-	-/-	12	5.77	6.25
+/Zα	+/+	18	8.65	6.25
+/Zα	+/-	25	12.02	12.5
+/Zα	-/-	8	3.85	6.25
Zα/-	+/+	12	5.77	6.25
Zα/-	+/-	19	9.13	12.5
Zα/-	-/-	9	4.33	6.25

c

	Adar$^{Zα/-}$		
Ripk3:	+/+	+/-	-/-
≤ P2	8	10	8
> P2	0	2*	1#

**died at P3 and # at P6*

d

Breeding: *Adar*$^{+/-}$ *Mlkl*$^{-/-}$ X *Adar*$^{+/Zα}$ *Mlkl*$^{-/-}$

Adar	*Mlkl*	n	obs.%	exp.%
+/+	-/-	9	26.5	25.0
+/-	-/-	10	29.4	25.0
+/Zα	-/-	9	26.5	25.0
Zα/-	-/-	6	17.7	25.0

e

Breeding: *Adar*$^{+/-}$ *Mlkl*$^{-/-}$ X *Adar*$^{Zα/Zα}$ *Mlkl*$^{-/-}$

	Mlkl	n	obs.%	exp.%
+/Zα	-/-	31	57.4	50.0
Zα/-	-/-	23	42.6	50.0

f

Breeding: *Adar*$^{+/-}$ *Mlkl*$^{-/-}$ *Casp8*$^{+/-}$ X *Adar*$^{+/Zα}$ *Mlkl*$^{-/-}$ *Casp8*$^{+/-}$

Adar	*Mlkl*	*Casp8*	n	obs.%	exp.%
+/+	-/-	+/+	5	7.46	6.25
+/+	-/-	+/-	9	13.4	12.5
+/+	-/-	-/-	4	5.97	6.25
+/-	-/-	+/+	5	7.46	6.25
+/-	-/-	+/-	8	12.0	12.5
+/-	-/-	-/-	9	13.4	6.25
+/Zα	-/-	+/+	3	4.48	6.25
+/Zα	-/-	+/-	12	18.0	12.5
+/Zα	-/-	-/-	4	5.97	6.25
Zα/-	-/-	+/+	0	0.00	6.25
Zα/-	-/-	+/-	7	10.5	12.5
Zα/-	-/-	-/-	1	1.49	6.25

g

Breeding: *Adar*$^{+/-}$ *Mlkl*$^{-/-}$ *Casp8*$^{+/-}$ X *Adar*$^{Zα/Zα}$ *Mlkl*$^{-/-}$ *Casp8*$^{+/-}$

Adar	*Mlkl*	*Casp8*	n	obs.%	exp.%
+/Zα	-/-	+/+	6	7.59	12.5
+/Zα	-/-	+/-	26	33.0	25.0
+/Zα	-/-	-/-	10	12.7	12.5
Zα/-	-/-	+/+	5	6.33	12.5
Zα/-	-/-	+/-	27	34.2	25.0
Zα/-	-/-	-/-	5	6.33	12.5

h

	Adar$^{Zα/-}$ *Mlkl*$^{-/-}$		
Casp8:	+/+	+/-	-/-
≤ P2	19	17	3
> P2	0	0	0

Extended Data Fig. 9 | Characterisation of *Adar*$^{Zα/-}$ *Ripk3*$^{-/-}$ and *Adar*$^{Zα/-}$ *Mlkl*$^{-/-}$ *Casp8*$^{-/-}$ mice. a, Sections from ileum or jejunum of *Adar*$^{+/Zα}$ *Zbp1*$^{+/+}$ and *Adar*$^{Zα/-}$ *Zbp1*$^{+/+}$ or *Zbp1*$^{Zα1Zα2/Zα1Zα2}$ mice stained for cleaved caspase-8 (D387) and counterstained with haematoxylin. Scale bars = 100 µm. At least 3 mice per genotype were analysed. **b**, Numbers (n) and percentages of pups obtained from interbreeding of *Adar*$^{+/-}$ *Ripk3*$^{+/-}$ X *Adar*$^{+/Zα}$ *Ripk3*$^{+/-}$ mice. **c**, Number of *Adar*$^{Zα/-}$ *Ripk3*$^{+/+}$, *Adar*$^{Zα/-}$ *Ripk3*$^{+/-}$ or *Adar*$^{Zα/-}$ *Ripk3*$^{-/-}$ that survived beyond day 2 after birth (> P2). **d**, Numbers and percentages of pups obtained from interbreeding of *Adar*$^{+/-}$ *Mlkl*$^{-/-}$ X *Adar*$^{+/Zα}$ *Mlkl*$^{-/-}$ mice. **e**, Numbers and percentages of pups obtained from interbreeding of *Adar*$^{+/-}$ *Mlkl*$^{-/-}$ X *Adar*$^{Zα/Zα}$ *Mlkl*$^{-/-}$ mice. **f**, Numbers and percentages of pups obtained from interbreeding of *Adar*$^{+/-}$ *Mlkl*$^{-/-}$ *Casp8*$^{+/-}$ X *Adar*$^{+/Zα}$ *Mlkl*$^{-/-}$ *Casp8*$^{+/-}$ mice. **g**, Numbers and percentages of pups obtained from interbreeding of *Adar*$^{+/-}$ *Mlkl*$^{-/-}$ *Casp8*$^{+/-}$ X *Adar*$^{Zα/Zα}$ *Mlkl*$^{-/-}$ *Casp8*$^{+/-}$ mice. **h**, Number of *Adar*$^{Zα/-}$ *Mlkl*$^{-/-}$ *Casp8*$^{+/+}$, *Adar*$^{Zα/-}$ *Mlkl*$^{-/-}$ *Casp8*$^{+/-}$ or *Adar*$^{Zα/-}$ *Mlkl*$^{-/-}$ *Casp8*$^{-/-}$ mice that survived beyond day 2 after birth (> P2).

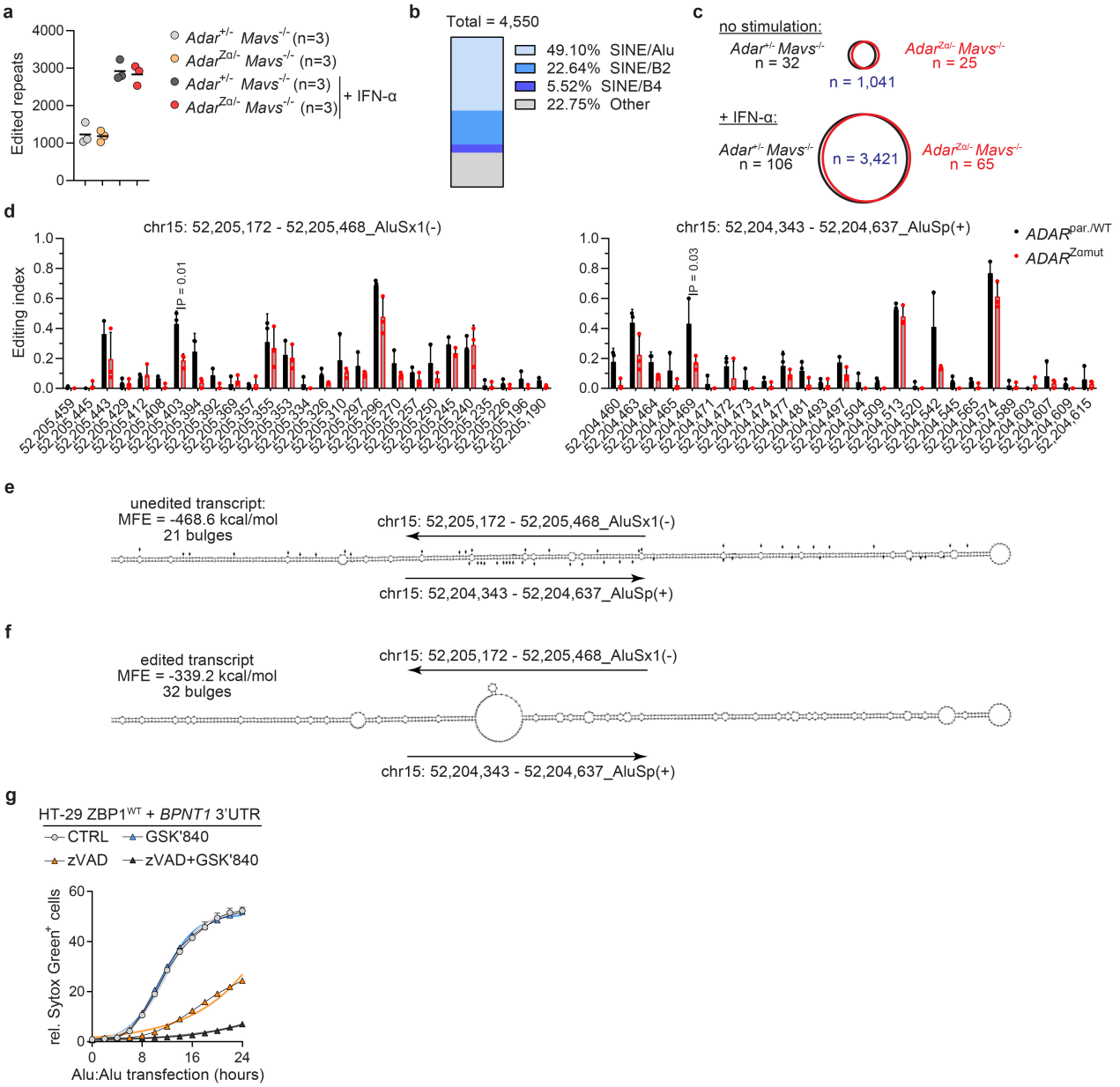

Extended Data Fig. 10 | A-to-I editing analysis of mRNA in mouse and human ADAR1 Zα domain mutant cells. a, Primary lung fibroblasts derived from mice of the indicated genotypes were stimulated for 16 h with 200 U/mL IFN-α or left untreated. The total number of mouse repeat elements that underwent A-to-I editing was determined for 3 independent cell lines per genotype. Lines represent the mean. **b**, Boxplot illustrating the distribution of repeat elements in which editing activity was observed in 3 individual cell lines per genotype treated or not with IFN-α as indicated in **(a)**. **c**, Venn diagrams displaying the number of repeat elements of which A-to-I editing activity was restricted to a single genotype (*Adar*$^{+/-}$ *Mavs*$^{-/-}$ or *Adar*$^{Zα/-}$ *Mavs*$^{-/-}$) or those that were detected in both groups without stimulation or following IFN-α treatment as indicated in **(a)**. **d**, Graphical representation of the differential A-to-I editing profile of *ADAR*$^{Par/WT}$ and *ADAR*^{Zαmut} HEK293 cells detected on the indicated AluSp element in Fig. 4c and its nearest inverted repeat element (AluSx1). Data points show mean + SD; P values by Welch's t-test. **e**,**f**, The RNAfold webtool was used to predict the folding structure and minimum free energy (MFE) of dsRNA formed by the AluSp:AluSx1 hybrid in complete absence of A-to-I editing **(e)** and when fully edited **(f)** at the A-to-I sites identified in **(d)**. The A-to-I editing sites are indicated with black arrows. **g**, Transfection of HT-29 ZBP1^{WT} with 50 ng of *BPNT1* 3'UTR duplex RNA in combination with 3 μM GSK'840 and/or 20 μM zVAD-fmk. Cell death was analysed as in Fig. 3d. Fitted lines represent a logistic growth fit. Data points show the mean of 2 technical replicates + SD and are representative of 3 independent experiments.

nature portfolio

Corresponding author(s): Jonathan Maelfait

Last updated by author(s): May 16, 2022

Reporting Summary

Nature Portfolio wishes to improve the reproducibility of the work that we publish. This form provides structure for consistency and transparency in reporting. For further information on Nature Portfolio policies, see our Editorial Policies and the Editorial Policy Checklist.

Statistics

For all statistical analyses, confirm that the following items are present in the figure legend, table legend, main text, or Methods section.

n/a	Confirmed	
☐	☒	The exact sample size (*n*) for each experimental group/condition, given as a discrete number and unit of measurement
☐	☒	A statement on whether measurements were taken from distinct samples or whether the same sample was measured repeatedly
☐	☒	The statistical test(s) used AND whether they are one- or two-sided *Only common tests should be described solely by name; describe more complex techniques in the Methods section.*
☐	☒	A description of all covariates tested
☐	☒	A description of any assumptions or corrections, such as tests of normality and adjustment for multiple comparisons
☒	☐	A full description of the statistical parameters including central tendency (e.g. means) or other basic estimates (e.g. regression coefficient) AND variation (e.g. standard deviation) or associated estimates of uncertainty (e.g. confidence intervals)
☐	☒	For null hypothesis testing, the test statistic (e.g. *F*, *t*, *r*) with confidence intervals, effect sizes, degrees of freedom and *P* value noted *Give P values as exact values whenever suitable.*
☒	☐	For Bayesian analysis, information on the choice of priors and Markov chain Monte Carlo settings
☒	☐	For hierarchical and complex designs, identification of the appropriate level for tests and full reporting of outcomes
☒	☐	Estimates of effect sizes (e.g. Cohen's *d*, Pearson's *r*), indicating how they were calculated

Our web collection on statistics for biologists contains articles on many of the points above.

Software and code

Policy information about availability of computer code

Data collection	Cell death data was collected by using an IncuCyte ZOOM Live-cell Analysis system (Sartorius). Quantitative Reverse-transcription PCR data was obtained by LightCycler 480 system (Roche). Microscopy images were acquired on a Zeiss LSM880 Fast Airyscan confocal microscope and Zeiss Axio Scan slide scanner. Western blot data was collected by Amersham Imager 600 (GE Healthcare Life Sciences). Flow cytometry data was collected by LSRFortessa or FACSymphony instruments (BD Biosciences). RNA sequencing was performed on an Illumina Novaseq6000 .
Data analysis	Statistical analysis was performed with Graphpad Prism V8. Cell death assay data was analyzed with IncuCyte ZOOM 2018A (Sartorius). Micropscopy images were analyzed using ZEN software (Zeiss) and ImageJ/Fiji (NIH). Flow cytometry data was analyzed using FlowJo software (Tree Star). RNA sequencing data was analysed using the pipeline made available on GitHub (https://github.com/vibbits/rnaseq-editing), further downstream processing steps were performed in R (version 4.1.1). In silico RNA folding analysis was done using the RNAfold webtool from the Vienna RNA Websuite.

For manuscripts utilizing custom algorithms or software that are central to the research but not yet described in published literature, software must be made available to editors and reviewers. We strongly encourage code deposition in a community repository (e.g. GitHub). See the Nature Portfolio guidelines for submitting code & software for further information.

Data

Policy information about availability of data

All manuscripts must include a data availability statement. This statement should provide the following information, where applicable:

- Accession codes, unique identifiers, or web links for publicly available datasets
- A description of any restrictions on data availability
- For clinical datasets or third party data, please ensure that the statement adheres to our policy

Raw data of flow cytometry experiments, RT-qPCR, microscopy or uncropped Western blot images are available upon request. Raw RNA sequencing data used in this study is available on the European Nucleotide Archive (https://www.ebi.ac.uk/ena/browser/home), accession codes PRJEB52610 and PRJEB52618.

Field-specific reporting

Please select the one below that is the best fit for your research. If you are not sure, read the appropriate sections before making your selection.

☒ Life sciences ☐ Behavioural & social sciences ☐ Ecological, evolutionary & environmental sciences

For a reference copy of the document with all sections, see nature.com/documents/nr-reporting-summary-flat.pdf

Life sciences study design

All studies must disclose on these points even when the disclosure is negative.

Sample size	No sample size calculations were performed. Whenever possible, tissues and cells from at least 3 animals per genotype were analysed to be sure differences were reproducible.
Data exclusions	No data was excluded from the analysis.
Replication	Whenever possible, experiments were performed with at least 3 mice of the indicated genotypes. In vitro experiments were replicated at least 2 times for cell death assays (with 2 or 3 technical replicates per experiment) and at least 2 times for immunoblotting experiments.
Randomization	Allocation of groups was not random and determined by the genotype of the mice. Animals were age-, but not sex-matched.
Blinding	Investigators were not blinded during data collection as the group allocation was determined by the genotype of the mice. Histological evaluation of TUNEL data was performed blindly.

Reporting for specific materials, systems and methods

We require information from authors about some types of materials, experimental systems and methods used in many studies. Here, indicate whether each material, system or method listed is relevant to your study. If you are not sure if a list item applies to your research, read the appropriate section before selecting a response.

Materials & experimental systems

n/a	Involved in the study
☐	☒ Antibodies
☐	☒ Eukaryotic cell lines
☒	☐ Palaeontology and archaeology
☐	☒ Animals and other organisms
☒	☐ Human research participants
☒	☐ Clinical data
☒	☐ Dual use research of concern

Methods

n/a	Involved in the study
☒	☐ ChIP-seq
☐	☒ Flow cytometry
☒	☐ MRI-based neuroimaging

Antibodies

Antibodies used

Immunoblotting
Mouse monoclonal anti-mouse ZBP1 (Zippy-1), Adipogen Cat# AG-20B-0010, RRID:AB_2490191, 1/2000
Mouse monoclonal anti-human Caspase-8 P.H. Krammer lab, 1/1000
Rabbit polyclonal anti-human ZBP1, Cell Signaling Technology Cat# 60968, RRID:AB_2799599, 1/1000
Rabbit monoclonal anti-human ADAR1 (D7E2M), Cell Signaling Technology Cat# 14175, RRID:AB_2722520, 1/1000
Rabbit polyclonal anti-mouse/human β-Tubulin-HRP, Abcam Cat# ab21058, RRID:AB_727045, 1/10000
Rabbit polyclonal anti-human MLKL, GeneTex Cat# GTX107538, RRID:AB_2037439, 1/1000
Rabbit monoclonal anti-human MLKL (phospho S358), Abcam Cat# ab187091, RRID:AB_2619685, 1/1000
Rabbit polyclonal anti-mouse ADAR1 p150, Synaptic Systems Cat# 293 003, RRID:AB_2620031, 1/1000

Rabbit polyclonal anti-human ADAR1 p150, Bethyl Cat#A303-883A, RRID:AB_2620233, 1/1000
Rabbit polyclonal anti-mouse MAVS, Cell Signaling Technology Cat# 4983, RRID:AB_823566, 1/1000
Rabbit polyclonal anti-mouse RIPK3, ProSci Cat# 2283, RRID:AB_203256, 1/1000
Rabbit monoclonal anti-mouse Cleaved Caspase-8 (Asp387), Cell Signaling Technology Cat# 8592, RRID:AB_10891784, 1/1000
Rabbit monoclonal anti-human RIP1 (D94C12) XP, Cell Signaling Technology Cat# 3493, RRID:AB_2305314, 1/1000
Rabbit polyclonal anti-human TRIF, Cell Signaling Technology Cat# 4596, RRID:AB_2256555, 1/1000
Rabbit monoclonal anti-human RIPK3 (E7A7F) XP, Cell Signaling Technology Cat# 10188, RRID:AB_2904619, 1/1000
Rabbit monoclonal anti-mouse MLKL (phospho S345) (D6E3G), Cell Signaling Technology Cat# 37333, RRID:AB_2799112, 1/1000
Rat monoclonal anti-mouse MLKL (3H1), Milipore Cat# MABC604, RRID:AB_2820284, 1/1000
Donkey anti-rabbit IgG - HRP, GE Healthcare Cat# NA934, RRID:AB_772206, 1/5000
Sheep anti-mouse IgG - HRP, GE Healthcare Cat# NA931, RRID:AB_772210, 1/5000
Goat anti-rat IgG - HRP, GE Healthcare Cat# NA935, RRID:AB_77220, 1/5000

Flow cytometry
Annexin V#APC, BD Biosciences Cat# 550475, RRID:AB_2868885, 1:200
Fixable Viability#eFluor506, Thermo Fisher Scientific Cat# 65-0866-14, 1:200
anti-mouse CD16/CD32 (Fc block, clone 2.4G2), BD Biosciences Cat# 553142, RRID:AB_394657, 1:200
anti-mouse CD3e#BUV395 (clone 145-2C11), BD Biosciences Cat# 563565, RIDD:AB_2738278, 1:100
anti-mouse CD4#BUV735 (clone GK1.5), BD Biosciences Cat# 564298, RRID:AB_2738734, 1:400
anti-mouse CD8a#eFluor450 (clone 53-6.7), Thermo Fisher Scientific Cat# 48-0081-82, RRID:AB_1272198, 1:400
anti-mouse CD8a#FITC (clone 53-6.7), BioLegend Cat# 100705, RRID:AB_312744, 1:800
anti-mouse CD161/NK-1.1#BV605 (clone PK136), BD Biosciences Cat# 563220, RRID:AB_2738077, 1:300
anti-mouse CD64#BV711 (clone X54-5/7.1), BioLegend Cat# 139311, RRID:AB_2563846, 1:100
anti-mouse Ly-6G#BV785 antibody (clone 1A8), Biolegend Cat#127645; RRID: AB_2566317, 1:400
anti-mouse MHC Class II (I-A/I-E)#FITC (clone M5/114.15.2), eBioscience Cat#11-5321-82; RRID: AB_465232, 1:1000
anti-mouse CD11b#PerCP-Cy5.5 (clone M1/70), BD Biosciences Cat#550993; RRID: AB_394002, 1:1000
anti-mouse CD11b#APC-eFluor780 (clone M1/70), Thermo Fisher Scientific Cat# 47-0112-80, RRID:AB_1603195, 1:500
anti-mouse γδ T-Cell Receptor#PE-CF594 (clone GL3), BD Biosciences Cat# 563532, RRID:AB_2661844, 1:500
anti-mouse CD11c#PE-Cy7 (clone N418), Thermo Fisher Scientific Cat# 25-0114-82, RRID:AB_469590, 1:500
anti-mouse F4/80#APC (clone BM8), Thermo Fisher Scientific Cat# 17-4801, RRID:AB_469452, 1:200
anti-mouse CD45#AlexaFluor700 (clone 30-F11), Thermo Fisher Scientific Cat# 56-0451-80, RRID:AB_891456, 1:200
anti-mouse TCR β chain#APC-Cy7 (clone H54-597), BioLegend Cat# 109220, RRID:AB_893624, 1:200
anti-mouse CD172a#PerCP-eFluor710 (clone P84), Thermo Fisher Scientific Cat# 46-1721-80, RRID:AB_10805866, 1:200
anti-mouse/rat XCR1#PE (clone ZET), BioLegend Cat# 148203, RRID:AB_2563842, 1:400
anti-mouse CD19#PE-Cy5 (clone eBio1D3), Thermo Fisher Scientific Cat# 15-0193-82, RRID:AB_657672, 1:500
anti-mouse CD19#AlexaFluor700 (clone eBio1D3), Thermo Fisher Scientific Cat# 56-0193-80, RRID:AB_837082, 1:600
anti-mouse Siglec-F#BV421 (clone E50-2440), BD Biosciences Cat#565934; RRID: AB_2739398, 1:400
anti-mouse CD200R3#PE (clone Ba13), BioLegend Cat# 142205, RRID:AB_10915271, 1:300
anti-mouse Ly-6C#APC-Cy7 (clone AL-21), BD Biosciences Cat# 560596, RRID:AB_1727555, 1:100

Histology
Goat anti-Rabbit IgG Antibody (H+L), Biotinylated, Vector, Cat# BA-1000, RRID:AB_2231606 1/300
Rabbit monoclonal anti-mouse Cleaved Caspase-8 (Asp387), Cell Signaling Technology Cat# 8592, RRID:AB_10891784, 1/500
Rabbit polyclonal anti-mouse Keratin 5 (AF 138), Covance Cat# PRB-160P-100, RRID:AB_291581, 1/1000
Goat Anti-Rabbit IgG antibody (DyLight488), GeneTex Cat# GTX213110-04, RRID:AB_2887579, 1/1000

Validation

All antibodies are commercially available and have been verified by the manufacturers. Validation data for all antibodies are available on vendors websites.

Eukaryotic cell lines

Policy information about cell lines

Cell line source(s)

Primary cells (lung fibroblasts) were derived from the mice. HEK293, HEK293T and HT-29 cells were purchased from ATCC (Cat. CRL-1573, CRL-3216 and HTB-38 respectively).

Authentication

Primary lung fibroblasts were derived from mice and cultured for a limited number of passages. Genotypes were confirmed by Western blotting. Cell lines from ATCC have been authenticated by ATCC.

Mycoplasma contamination

Absence of mycoplasma contamination was regularly confirmed for mouse-derived primary lung fibroblast cultures, HT-29 and HEK293(T) cells.

Commonly misidentified lines
(See ICLAC register)

No ICLAC cell lines were used in this study.

Animals and other organisms

Policy information about studies involving animals; ARRIVE guidelines recommended for reporting animal research

Laboratory animals

C57BL/6 male and female embryos (E10.5-E13.5) and mice (P0.5-53 weeks of age) of the indicated genotypes were used in this study.

Wild animals

The study did not involve wild animals.

Field-collected samples

The study did not involve field-collected samples.

Ethics oversight	All animal experiments were conducted following approval by the local Ethics Committee of the Ghent University.

Note that full information on the approval of the study protocol must also be provided in the manuscript.

Flow Cytometry

Plots

Confirm that:

☒ The axis labels state the marker and fluorochrome used (e.g. CD4-FITC).

☒ The axis scales are clearly visible. Include numbers along axes only for bottom left plot of group (a 'group' is an analysis of identical markers).

☒ All plots are contour plots with outliers or pseudocolor plots.

☒ A numerical value for number of cells or percentage (with statistics) is provided.

Methodology

Sample preparation	Spleen and peripheral blood processing Spleens were collected in ice-cold PBS and digested for 30 min at 37°C in digestion buffer (RPMI-1640 supplemented 0.5 mg/ml collagenase D and 10 mg/ml DNase I) with regular mixing. After neutralization with RPMI-1640 medium containing FCS, erythrocytes were lysed the digest was filtered through a 70 mm cell strainer to obtain single cell solutions. Peripheral blood was collected in EDTA-coated tubes by tail vein bleeding. Next, erythrocytes were lysed for 10 minutes and cells were washed 2 times with ice-cold PBS and were stained for flow cytometry analysis. Skin processing A piece of shaved mouse skin (±12 cm2) was isolated from 3 wk-old mice. Subcutaneous fat and muscles were removed by mechanical scrapping with a scalpel. Subsequently, the skin was placed on 0.4 mg/ml Dispase II (Roche; 4492078001) with the dermal side facing downward for 2 h at 37°C. Epidermis was separated from the dermis with a forceps, cut into fine pieces, and incubated in 2 ml enzymatic solution containing 1.5 mg/ml collagenase type IV (Worthington; LS004188) and 0.5 mg/ml Dnase I (Roche; 10104159001) for 20 min at 37°C with shaking. After neutralization with FCS, the cell suspension was filtered through a 70 µm cell strainer to obtain a single cell suspension.
Instrument	LSR Fortessa and FACSymphony (BD Biosciences)
Software	Flow cytometry data was analyzed using FlowJo software (Tree Star).
Cell population abundance	*Describe the abundance of the relevant cell populations within post-sort fractions, providing details on the purity of the samples and how it was determined.*
Gating strategy	Positive and negative gates were set using fluorescence minus one (FMO) background intensity controls. Detailed gating strategy is provided in the Extended Data Figures of the manuscript.

☒ Tick this box to confirm that a figure exemplifying the gating strategy is provided in the Supplementary Information.